JOURNAL OF GUIDANCE, CONTROL, AND DYNAMICS
Vol. 40, No. 12, December 2017

Fast and Near-Optimal Guidance for Docking to Uncontrolled Spacecraft

Jacopo Ventura*
Technical University of Munich, 85748 Garching, Germany
Marco Ciarcià† and Marcello Romano‡
Naval Postgraduate School, Monterey, 93940 California
and
Ulrich Walter§
Technical University of Munich, 85748 Garching, Germany

DOI: 10.2514/1.G001843

This paper proposes a guidance scheme for autonomous docking between a controlled spacecraft and an uncontrolled tumbling target in circular orbit. The onboard trajectory planning consists of a direct optimization method based on the inversion of the system dynamics. The trajectory components of the controlled spacecraft are imposed by using polynomial functions. Some of the polynomial coefficients are constrained to satisfy path constraints, whereas the remaining coefficients are varied parameters to be optimized. The optimal control problem is converted into a nonlinear programming problem by inverting the system dynamics. The proposed guidance scheme, based on the closed-loop implementation of this optimization problem, is applied to several scenarios. The resulting trajectories closely match the solutions of the correspondent optimal control problems. The guidance scheme is shown to perform precise maneuvers in most maneuvering situations, even in the presence of orbital perturbations. The sensitivity analysis to system uncertainties shows that the guidance is sensitive to noise on the target angular velocity, being the critical disturbance for this type of maneuvers.

Nomenclature

$\boldsymbol{b}$	=	boresight direction vector of the chaser rendezvous sensor
C	=	principal body-fixed Cartesian coordinate system of the chaser spacecraft
CD	=	auxiliary body-fixed Cartesian coordinate system on the chaser docking point
$\boldsymbol{F}$	=	control thrust vector, N
H	=	Hill Cartesian coordinate system
I^s_{xx}, I^s_{yy}, I^s_{zz}	=	moments of inertia of the spacecraft s about the principal axes (s equal to C, T), $\mathrm{kg \cdot m^2}$
J	=	performance index of the optimal control problem
$\boldsymbol{l}^s$	=	position of the spacecraft's docking point expressed in the system s (s equal to C, T), m
m_{C}	=	mass of the chaser spacecraft, kg
$\boldsymbol{q}^{\mathrm{T}}$	=	quaternion vector of the attitude of the target principal system with respect to the Hill system
$\boldsymbol{R}^{\mathrm{B}}_{\mathrm{A}}$	=	direction cosine matrix, from the coordinate system A to the system B
$\boldsymbol{r}$	=	position vector of the spacecraft center of mass with respect to the inertial coordinate system, m
r_{safe}	=	safety radius for collision avoidance, m
$\boldsymbol{s}$	=	position vector of the chaser rendezvous sensors with respect to the chaser center of mass, m
T	=	principal body-fixed Cartesian coordinate system of the target spacecraft
$\boldsymbol{T}$	=	control torque vector, $\mathrm{N \cdot m}$
TD	=	auxiliary body-fixed Cartesian coordinate system on the target docking point
t_{f}	=	maneuver duration, s
t_{GNC}	=	period of execution of the guidance loop, s
$t_{\min}$	=	sampling rate of the low-level attitude and position controllers, s
$\boldsymbol{v}_{\mathrm{con}}$	=	contact velocity between chaser and target docking points, m/s
$\boldsymbol{x}$	=	state vector of the two-spacecraft rendezvous model
x, y, z	=	position of the chaser center of mass expressed in the Hill coordinate system, m
α_{FOV}	=	half-angle of the rendezvous sensor field-of-view cone, rad
α_T	=	angular distance from the rendezvous sensor boresight to the target spacecraft center of mass, rad
$\Delta \boldsymbol{r}$	=	relative distance between docking points at the docking instant, m
$\Delta \boldsymbol{v}$	=	relative velocity between docking points at the docking instant, m
$\Delta \boldsymbol{\theta}$	=	relative attitude (Euler angles 1-2-3) between auxiliary systems CD and TD at the docking instant, deg
$\Delta \boldsymbol{\omega}$	=	relative angular velocity between auxiliary systems CD and TD at the docking instant, deg/s
δa	=	noise applied to the variable a
$\boldsymbol{\sigma}^{\mathrm{C}}$	=	modified Rodrigues parameters vector of the attitude of the chaser principal system with respect to the Hill system
Ω	=	angular velocity of the Hill coordinate system with respect to the inertial frame, rad/s
$\boldsymbol{\omega}^s$	=	angular velocity of the spacecraft s with respect to the inertial coordinate system (s equal to C, T), rad/s
${}^{\mathrm{H}}\boldsymbol{\omega}^s$	=	angular velocity of the spacecraft s with respect to the Hill coordinate system (s equal to C, T), rad/s

Received 7 November 2015; revision received 5 April 2016; accepted for publication 5 April 2016; published online 9 September 2016.

*Ph.D. Candidate, Institute of Astronautics, Boltzmannstraße 15.

†NRC Research Associate, Department of Mechanical and Aerospace Engineering, 700 Dyer Road, Watkins Hall. Member AIAA.

‡Associate Professor, Department of Mechanical and Aerospace Engineering, 700 Dyer Road, Watkins Hall. Associate Fellow AIAA.

§Head, Institute of Astronautics, Boltzmannstraße 15.

Subscripts

0	=	value at the beginning of the maneuver
f	=	value at the end of the maneuver
t	=	value at the particular instant of time t

Superscript

s	=	vector whose components are expressed in the coordinate system s (s equal to H, C, CD, T, TD)

I. Introduction

RENDEZVOUS and docking operations between spacecraft are key maneuvers in spaceflight. The capability of two spacecraft to mechanically connect to each other enabled missions such as the Apollo program for moon exploration, the servicing flights of the Space Shuttle, and the assembly and supply of the space stations [1]. In these missions, the docking procedures have been mainly performed by crewed space vehicles and involved cooperative target spacecraft (i.e., its attitude was controlled to help the maneuver execution).

Recently, the main efforts have been focused on developing spacecraft rendezvous technologies for autonomous proximity flights and docking operations. This research has been motivated by the new generation of space missions such as debris removal and robotic on-orbit servicing to repair, refuel, and upgrade disabled spacecraft [2,3]. The desired outcome of performing autonomous missions is the increment of mission frequency, robustness, and reliability with respect to the existing ground-in-the-loop guidance methods [4]. Furthermore, the capability to autonomously rendezvous and dock allows to retrieve and service a variety of target spacecraft being either cooperative or noncooperative. Cooperative targets employ attitude control system to stabilize their attitude and enable features allowing the chaser to estimate the relative state between spacecraft. Noncooperative targets, on the contrary, do not assist the chaser during the maneuver because they are not equipped with dedicated docking features, and their attitude is not controlled. Examples of noncooperative targets are space debris or end-of-life spacecraft, which represent the majority of targets for on-orbit servicing and space debris removal missions [2]. Consequently, the main challenge for these new generation missions is to autonomously dock to noncooperative targets, which may tumble around their principal axes.

Spacecraft rendezvous technologies for autonomous inspection and docking have been recently tested in demonstration missions. The Engineering Test Satellite No. 7 performed both autonomous and remote controlled docking to a cooperative/stabilized target [5]. However, the maneuvers were performed after overcoming problems in the filter of the attitude control software that caused the loss of the chaser attitude. The Experimental Satellite System 10 (XSS-10) and XSS-11, commissioned by the U.S. Air Force Research Laboratory, demonstrated the capability of a microsatellite to safely and autonomously rendezvous and inspect multiple noncooperative space objects [6]. In 2005, the NASA Demonstration of Autonomous Rendezvous Test missions was launched to perform autonomous close proximity operations [7,8]. Here, the maneuver failed due to an anomaly in the navigation software. The Orbital Express program, developed by the U.S. Defense Advanced Research Projects Agency, successfully performed for the first time several fully autonomous approaches and captures of a cooperative target in 2007 [4,9]. Notably, in this mission, the target spacecraft attitude was completely stabilized. The Swedish National Space Board together with DLR, German Aerospace Center launched the PRISMA mission in 2010. Here, the servicer successfully performed an autonomous rendezvous maneuver from 30 km to the final hold point at 3 km of relative distance to the noncooperative target [10]. However, technologies enabling autonomous docking to uncontrolled targets still have to be demonstrated in orbit.

Concerning optimal guidance strategies for autonomous rendezvous and docking to an uncontrolled target, significant achievements have been attained in the last decade. The model predictive control approach is employed by several authors to generate feasible docking trajectories [11–13]. Notably, Di Cairano [13] applies a linear-quadratic model predictive control to generate online suboptimal planar trajectories to approach a tumbling object. However, in these works, the six-degree-of-freedom (6-DOF) maneuver is not addressed. An optimizing path planner for planar rendezvous maneuvers is proposed in [14]. This approach uses a genetic algorithm to optimize the trajectory with respect to the fuel expenditure. Breger and How [15] propose a technique based on the model predictive control method for onboard generation of fuel-optimal rendezvous trajectories that guarantees collision avoidance under thruster failures. Nolet [16] performs autonomous docking to a cooperative tumbling target using the SPHERES system. Here, the guidance algorithm employs the glide-slope method for rapid trajectory generation, disregarding both optimality and path constraints. Recently, Boyarko et al. [17] formulate the optimal control problem for the 6-DOF docking maneuver between a controlled spacecraft and a tumbling object. Based on this work, the same authors apply the inverse dynamics in the virtual domain method for rapid suboptimal docking trajectory generation [18]. Although this method is robust to numerous initial conditions, the high computational time required to generate the trajectory does not allow onboard implementation of the algorithm in closed-loop fashion. Lu and Liu [19] and Liu and Lu [20] propose a second-order cone-programming-based methodology to solve the rendezvous and proximity operations problem. The main strengths of this algorithm are computational speed, robustness, suboptimality, capability to handle path constraints, and applicability to any orbit of the target spacecraft. However, the methodology is limited to the translational problem only. Kobilarov and Pellegrino [21] formulate a trajectory planning algorithm for autonomous docking between self-assembling nanosatellites. Although a simplified version of the proposed method is validated on an air-bearing-based test bed with cooperative docking maneuvers, these authors emphasize the need of robustness and sensitivity analysis of guidance algorithms for the 6-DOF scenario as future work.

The U.S. National Research Council considers a reliable and robust guidance algorithm for autonomous docking to uncontrolled tumbling objects as high-priority cross-cutting technology for the 2012–2021 decade and beyond [22]. Based on the state of the art and on the requirements for future robotic missions, the next-generation guidance algorithms must present the following key aspects [22].

1) *Optimality*: for any feasible trajectory, an optimal or near-optimal solution, which minimizes the fuel or energy consumption, is desired.

2) *Robustness* against orbital perturbations and sensor noise.

3) *Real-time implementable*: algorithms must be executable onboard and in real-time.

To answer to these requirements, this paper presents a guidance strategy for autonomous docking maneuvers to uncontrolled tumbling target spacecraft. The algorithm consists of an onboard trajectory planning that employs a direct optimization method based on the inversion of the system dynamics. By imposing a polynomial shape to both rotational and translational trajectories components of the chaser spacecraft, the optimal control problem for docking maneuvers is converted into an equivalent nonlinear programming problem having a reduced number of parameters to be optimized. Path constraints such as target pointing and collision avoidance are enforced. This trajectory optimization problem is then solved in closed-loop fashion using the current state of the spacecraft as initial conditions.

The main contribution of this work is a rapid trajectory generation algorithm for the full 6-DOF docking maneuver to an uncontrolled tumbling target achieved by combining the inverse dynamics approach and a sequential optimization algorithm; the methodology includes a procedure for the estimation of a feasible docking maneuver duration before the trajectory optimization. The proposed algorithm is implemented in closed-loop fashion to attain near-optimality of the resulting trajectory. Finally, the paper analyzes robustness of this guidance strategy to orbital perturbations, sensor noise, and model uncertainty because these issues are critical for realistic applications. Through this study, the applicability of the proposed guidance to noncooperative docking maneuvers is evaluated.

Numerical experiments with the proposed guidance strategy show that the controlled trajectories are close to the solution of the initial optimal control problem with perfect controls while respecting all the maneuver constraints. The algorithm is fast enough to allow onboard application in real-time, as the trajectory optimization can be repeated several times during the maneuver. Monte Carlo simulations show robustness to different maneuvering situations under the presence of orbital perturbation and system disturbances such as sensor noise and model uncertainties. However, the guidance system is sensitive to noise on the target angular velocity, thus being the most critical parameter for noncooperative maneuvers to tumbling targets.

The present paper is organized as follows. Section II defines the dynamics model for the docking maneuver between a controlled spacecraft and an uncontrolled object. The optimal control problem for this maneuver, including the required path constraints, is then formulated in the same section. Section III describes the trajectory-optimization algorithm for rapid trajectory generation. The implementation in closed-loop fashion of the proposed trajectory optimization algorithms is discussed in Sec. IV. The numerical experiments are reported in Sec. V. Section VI concludes the paper.

II. Docking Dynamics Model and Optimal Control Problem Formulation

This section summarizes the dynamics model for the rendezvous maneuver between a controlled chaser spacecraft and an uncontrolled target spacecraft in circular orbit. The optimal control problem for this maneuver is then formulated according to the work of [17].

Figure 1 shows a sketch of the geometry and coordinate systems of the target and the chaser spacecraft. For each vehicle, two body-fixed Cartesian coordinate systems are defined. The origin of the principal system is located at the center of mass of the spacecraft with the axis directed along the principal axis of inertia. The auxiliary coordinate system is centered at the vehicle's docking point, and it is defined in such a way that the z axis lies along the vehicle docking axis (outward direction for the chaser and inward direction for the target as in Fig. 1) and the x axis points to the top of the spacecraft. The y axis completes the right-hand rule. Figure 1 also illustrates the orbiting the Hill coordinate system H: the origin is placed at the center of mass of the target spacecraft, the x axis points toward the zenith, the y axis is directed along the velocity vector of the target spacecraft, and the z axis points the orbit normal. The Earth-Centered-Inertial (ECI) coordinate system is located at the center of mass of the Earth.

A. Dynamics Model of the Docking Maneuver

For close-range proximity maneuvers between two spacecraft, the translational motion of the chaser spacecraft center of mass is described in the Hill coordinate system by the Clohessy–Wiltshire differential equations [23]:

$$\ddot{x} = 2\Omega\dot{y} + 3\Omega^2 x + \frac{F_x^{\mathrm{H}}}{m_{\mathrm{C}}} \quad \ddot{y} = -2\Omega\dot{x} + \frac{F_y^{\mathrm{H}}}{m_{\mathrm{C}}} \quad \ddot{z} = -\Omega^2 z + \frac{F_z^{\mathrm{H}}}{m_{\mathrm{C}}} \tag{1}$$

The dynamics of the rotational motion of the chaser spacecraft is governed by Euler's equation, which, in scalar form and referenced to the chaser principal axes, can be expressed as [24]

$$\begin{aligned} \dot{\omega}_x^{\mathrm{C}} &= \frac{(I_{yy}^{\mathrm{C}} - I_{zz}^{\mathrm{C}})\omega_z^{\mathrm{C}}\omega_y^{\mathrm{C}} + T_x^{\mathrm{C}}}{I_{xx}^{\mathrm{C}}} \\ \dot{\omega}_y^{\mathrm{C}} &= \frac{(I_{zz}^{\mathrm{C}} - I_{xx}^{\mathrm{C}})\omega_z^{\mathrm{C}}\omega_x^{\mathrm{C}} + T_y^{\mathrm{C}}}{I_{yy}^{\mathrm{C}}} \\ \dot{\omega}_z^{\mathrm{C}} &= \frac{(I_{xx}^{\mathrm{C}} - I_{yy}^{\mathrm{C}})\omega_y^{\mathrm{C}}\omega_x^{\mathrm{C}} + T_z^{\mathrm{C}}}{I_{zz}^{\mathrm{C}}} \end{aligned} \tag{2}$$

Similarly, the rotational dynamics of the target spacecraft (assumed in unforced motion) is given by

$$\begin{aligned} \dot{\omega}_x^{\mathrm{T}} &= \frac{(I_{yy}^{\mathrm{T}} - I_{zz}^{\mathrm{T}})\omega_z^{\mathrm{T}}\omega_y^{\mathrm{T}}}{I_{xx}^{\mathrm{T}}} \\ \dot{\omega}_y^{\mathrm{T}} &= \frac{(I_{zz}^{\mathrm{T}} - I_{xx}^{\mathrm{T}})\omega_z^{\mathrm{T}}\omega_x^{\mathrm{T}}}{I_{yy}^{\mathrm{T}}} \\ \dot{\omega}_z^{\mathrm{T}} &= \frac{(I_{xx}^{\mathrm{T}} - I_{yy}^{\mathrm{T}})\omega_y^{\mathrm{T}}\omega_x^{\mathrm{T}}}{I_{zz}^{\mathrm{T}}} \end{aligned} \tag{3}$$

Among all the possible attitude representations, the orientation of the chaser spacecraft is described using the modified Rodrigues parameters (MRP). This choice is motivated by the fact that the inverse dynamics method, which is later applied for rapid docking trajectory generation, achieves better performance (in terms of optimality and computational speed) when applied to MRP rather than quaternions or Euler angles [25]. As a consequence, the attitude of the chaser principal axes with respect to the Hill system is expressed in terms of MRP $\boldsymbol{\sigma}^{\mathrm{C}} = [\sigma_1^{\mathrm{C}}, \sigma_2^{\mathrm{C}}, \sigma_3^{\mathrm{C}}]$ according to the following kinematic equation [26]:

$$\begin{aligned} &\begin{bmatrix} \dot{\sigma}_1^{\mathrm{C}} \\ \dot{\sigma}_2^{\mathrm{C}} \\ \dot{\sigma}_3^{\mathrm{C}} \end{bmatrix} \\ &= \frac{1}{4}\begin{bmatrix} 1+\sigma_1^{\mathrm{C}2}-\sigma_2^{\mathrm{C}2}-\sigma_3^{\mathrm{C}2} & 2(\sigma_1^{\mathrm{C}}\sigma_2^{\mathrm{C}}-\sigma_3^{\mathrm{C}}) & 2(\sigma_1^{\mathrm{C}}\sigma_3^{\mathrm{C}}+\sigma_2^{\mathrm{C}}) \\ 2(\sigma_1^{\mathrm{C}}\sigma_2^{\mathrm{C}}+\sigma_3^{\mathrm{C}}) & 1-\sigma_1^{\mathrm{C}2}+\sigma_2^{\mathrm{C}2}-\sigma_3^{\mathrm{C}2} & 2(\sigma_2^{\mathrm{C}}\sigma_3^{\mathrm{C}}-\sigma_1^{\mathrm{C}}) \\ 2(\sigma_1^{\mathrm{C}}\sigma_3^{\mathrm{C}}-\sigma_2^{\mathrm{C}}) & 2(\sigma_2^{\mathrm{C}}\sigma_3^{\mathrm{C}}+\sigma_1^{\mathrm{C}}) & 1-\sigma_1^{\mathrm{C}2}-\sigma_2^{\mathrm{C}2}+\sigma_3^{\mathrm{C}2} \end{bmatrix} \\ &\times \begin{bmatrix} {}^{\mathrm{H}}\omega_x^{\mathrm{C}} \\ {}^{\mathrm{H}}\omega_y^{\mathrm{C}} \\ {}^{\mathrm{H}}\omega_z^{\mathrm{C}} \end{bmatrix} = \frac{1}{4}\boldsymbol{B}(\boldsymbol{\sigma}^{\mathrm{C}})\,{}^{\mathrm{H}}\boldsymbol{\omega}^{\mathrm{C}} \end{aligned} \tag{4}$$

The components ${}^{\mathrm{H}}\omega_x^{\mathrm{C}}$, ${}^{\mathrm{H}}\omega_y^{\mathrm{C}}$, and ${}^{\mathrm{H}}\omega_z^{\mathrm{C}}$ of the chaser spacecraft angular velocity with respect to the Hill coordinate system and expressed in the chaser principal system C are obtained from $\boldsymbol{\omega}^{\mathrm{C}}$ with

$$\begin{bmatrix} {}^{\mathrm{H}}\omega_x^{\mathrm{C}} \\ {}^{\mathrm{H}}\omega_y^{\mathrm{C}} \\ {}^{\mathrm{H}}\omega_z^{\mathrm{C}} \end{bmatrix} = \begin{bmatrix} \omega_x^{\mathrm{C}} \\ \omega_y^{\mathrm{C}} \\ \omega_z^{\mathrm{C}} \end{bmatrix} - \boldsymbol{R}_{\mathrm{H}}^{\mathrm{C}} \begin{bmatrix} 0 \\ 0 \\ \Omega \end{bmatrix} \tag{5}$$

where

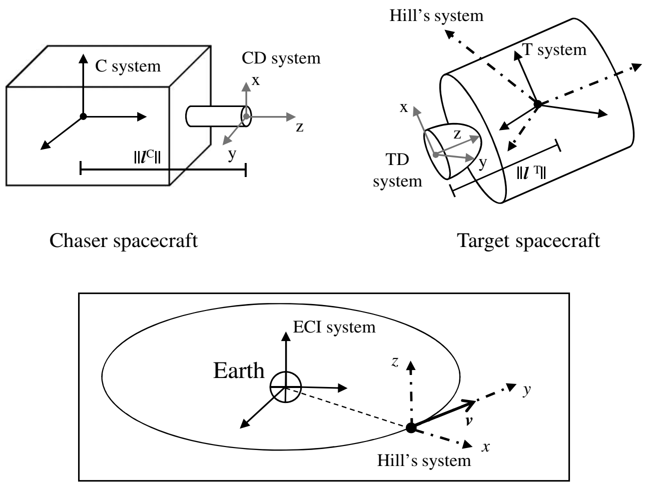

Chaser spacecraft

Target spacecraft

Fig. 1 Spacecraft geometry and coordinate systems.

$$\boldsymbol{R}_{\mathrm{H}}^{\mathrm{C}} = \frac{1}{(1+\boldsymbol{\sigma}^{\mathrm{C}}\cdot\boldsymbol{\sigma}^{\mathrm{C}})^2}\begin{bmatrix} 4(\sigma_1^{\mathrm{C}2}-\sigma_2^{\mathrm{C}2}-\sigma_3^{\mathrm{C}2})+\Sigma^2 & 8\sigma_1^{\mathrm{C}}\sigma_2^{\mathrm{C}}+4\sigma_3^{\mathrm{C}}\Sigma & 8\sigma_1^{\mathrm{C}}\sigma_3^{\mathrm{C}}-4\sigma_2^{\mathrm{C}}\Sigma \\ 8\sigma_1^{\mathrm{C}}\sigma_2^{\mathrm{C}}-4\sigma_3^{\mathrm{C}}\Sigma & 4(-\sigma_1^{\mathrm{C}2}+\sigma_2^{\mathrm{C}2}-\sigma_3^{\mathrm{C}2})+\Sigma^2 & 8\sigma_2^{\mathrm{C}}\sigma_3^{\mathrm{C}}+4\sigma_1^{\mathrm{C}}\Sigma \\ 8\sigma_1^{\mathrm{C}}\sigma_3^{\mathrm{C}}+4\sigma_2^{\mathrm{C}}\Sigma & 8\sigma_2^{\mathrm{C}}\sigma_3^{\mathrm{C}}-4\sigma_1^{\mathrm{C}}\Sigma & 4(-\sigma_1^{\mathrm{C}2}-\sigma_2^{\mathrm{C}2}+\sigma_3^{\mathrm{C}2})+\Sigma^2 \end{bmatrix} \tag{6}$$

is the direction cosine matrix from the Hill system H to the chaser principal system C in terms of MRP and

$$\Sigma = 1-\boldsymbol{\sigma}^{\mathrm{C}}\cdot\boldsymbol{\sigma}^{\mathrm{C}} \tag{7}$$

The attitude of the target principal axes with respect to the Hill coordinate system in terms of quaternion $\boldsymbol{q}^{\mathrm{T}} = [q_1^{\mathrm{T}}, q_2^{\mathrm{T}}, q_3^{\mathrm{T}}, q_4^{\mathrm{T}}]$ obeys the following kinematic differential equation [26]:

$$\begin{bmatrix} \dot{q}_1^{\mathrm{T}} \\ \dot{q}_2^{\mathrm{T}} \\ \dot{q}_3^{\mathrm{T}} \\ \dot{q}_4^{\mathrm{T}} \end{bmatrix} = \frac{1}{2}\begin{bmatrix} 0 & {}^{\mathrm{H}}\omega_z^{\mathrm{T}} & -{}^{\mathrm{H}}\boldsymbol{\omega}_y^{\mathrm{T}} & {}^{\mathrm{H}}\boldsymbol{\omega}_x^{\mathrm{T}} \\ -{}^{\mathrm{H}}\boldsymbol{\omega}_z^{\mathrm{T}} & 0 & {}^{\mathrm{H}}\boldsymbol{\omega}_x^{\mathrm{T}} & {}^{\mathrm{H}}\boldsymbol{\omega}_y^{\mathrm{T}} \\ {}^{\mathrm{H}}\boldsymbol{\omega}_y^{\mathrm{T}} & -{}^{\mathrm{H}}\boldsymbol{\omega}_x^{\mathrm{T}} & 0 & {}^{\mathrm{H}}\boldsymbol{\omega}_z^{\mathrm{T}} \\ -{}^{\mathrm{H}}\boldsymbol{\omega}_x^{\mathrm{T}} & -{}^{\mathrm{H}}\boldsymbol{\omega}_y^{\mathrm{T}} & -{}^{\mathrm{H}}\boldsymbol{\omega}_z^{\mathrm{T}} & 0 \end{bmatrix}\begin{bmatrix} q_1^{\mathrm{T}} \\ q_2^{\mathrm{T}} \\ q_3^{\mathrm{T}} \\ q_4^{\mathrm{T}} \end{bmatrix} \tag{8}$$

The components of the angular velocity vector ${}^{\mathrm{H}}\omega^{\mathrm{T}}$ are calculated by applying Eq. (5) to the target spacecraft. The expression of the direction cosine matrix from the Hill coordinate system to T in terms of quaternions is

$$\boldsymbol{R}_{\mathrm{H}}^{\mathrm{T}} = \begin{bmatrix} q_4^{\mathrm{T}2}+q_1^{\mathrm{T}2}-q_2^{\mathrm{T}2}-q_3^{\mathrm{T}2} & 2(q_1^{\mathrm{T}}q_2^{\mathrm{T}}+q_3^{\mathrm{T}}q_4^{\mathrm{T}}) & 2(q_1^{\mathrm{T}}q_3^{\mathrm{T}}-q_2^{\mathrm{T}}q_4^{\mathrm{T}}) \\ 2(q_1^{\mathrm{T}}q_2^{\mathrm{T}}-q_3^{\mathrm{T}}q_4^{\mathrm{T}}) & q_4^{\mathrm{T}2}-q_1^{\mathrm{T}2}+q_2^{\mathrm{T}2}-q_3^{T2} & 2(q_2^{\mathrm{T}}q_3^{\mathrm{T}}+q_1^{\mathrm{T}}q_4^{\mathrm{T}}) \\ 2(q_1^{\mathrm{T}}q_3^{\mathrm{T}}+q_2^{\mathrm{T}}q_4^{\mathrm{T}}) & 2(q_2^{\mathrm{T}}q_3^{\mathrm{T}}-q_1^{\mathrm{T}}q_4^{\mathrm{T}}) & q_4^{\mathrm{T}2}-q_1^{\mathrm{T}2}-q_2^{\mathrm{T}2}+q_3^{\mathrm{T}2} \end{bmatrix} \tag{9}$$

The dynamics model of the rendezvous maneuver between a controlled chaser spacecraft and an uncontrolled target spacecraft is defined by the differential set of Eqs. (1–8), and the state of the system becomes

$$\boldsymbol{x} = [x \;\; y \;\; z \;\; \dot{x} \;\; \dot{y} \;\; \dot{z} \;\; \omega_x^{\mathrm{C}} \;\; \omega_y^{\mathrm{C}} \;\; \omega_z^{\mathrm{C}} \;\; \sigma_1^{\mathrm{C}} \;\; \sigma_2^{\mathrm{C}} \;\; \sigma_3^{\mathrm{C}} \;\; \omega_x^{\mathrm{T}} \;\; \omega_y^{\mathrm{T}} \;\; \omega_z^{\mathrm{T}} \;\; q_1^{\mathrm{T}} \;\; q_2^{\mathrm{T}} \;\; q_3^{\mathrm{T}} \;\; q_4^{\mathrm{T}}] \tag{10}$$

To achieve a smooth physical contact between target and chaser docking points, it is necessary to enforce end conditions on both relative position and velocity [27]. More precisely, the chaser docking point must grapple the target docking point with a certain contact velocity $\boldsymbol{v}_{\mathrm{con}}^{\mathrm{C}}$ at the end of the maneuver. Furthermore, the chaser's auxiliary coordinate system CD must match the target's auxiliary system TD orientation and angular velocity. This ensures alignment of the docking axes and synchronization between the rotational motions of the docking points. Because contact shocks can be avoided by enforcement of suitable end conditions on just relative position and relative velocity, no final conditions on relative acceleration are considered in this paper. Accordingly, the docking-enabling conditions are expressed in terms of state variables as

$$\boldsymbol{R}_{\mathrm{T}}^{\mathrm{H}}\boldsymbol{l}^{\mathrm{T}} - \left(\boldsymbol{R}_{\mathrm{C}}^{\mathrm{H}}\boldsymbol{l}^{\mathrm{C}} + \begin{bmatrix} x_{\mathrm{f}} \\ y_{\mathrm{f}} \\ z_{\mathrm{f}} \end{bmatrix}\right) = 0 \tag{11}$$

$$\left(\boldsymbol{R}_{\mathrm{T}}^{\mathrm{H}}\boldsymbol{\omega}_{\mathrm{f}}^{\mathrm{T}} - \begin{bmatrix} 0 \\ 0 \\ \Omega \end{bmatrix}\right) \times \boldsymbol{R}_{\mathrm{T}}^{\mathrm{H}}\boldsymbol{l}^{\mathrm{T}} - \left\{\left(\boldsymbol{R}_{\mathrm{C}}^{\mathrm{H}}\boldsymbol{\omega}_{\mathrm{f}}^{\mathrm{C}} - \begin{bmatrix} 0 \\ 0 \\ \Omega \end{bmatrix}\right) \times \boldsymbol{R}_{\mathrm{C}}^{\mathrm{H}}\boldsymbol{l}^{\mathrm{C}} + \begin{bmatrix} \dot{x}_{\mathrm{f}} \\ \dot{y}_{\mathrm{f}} \\ \dot{z}_{\mathrm{f}} \end{bmatrix}\right\} = \boldsymbol{v}_{\mathrm{con}}^{\mathrm{H}} \tag{12}$$

$$\boldsymbol{R}_{\mathrm{TD}}^{\mathrm{H}} = \boldsymbol{R}_{\mathrm{CD}}^{\mathrm{H}} \tag{13}$$

$$\boldsymbol{R}_{\mathrm{T}}^{\mathrm{TDH}}\boldsymbol{\omega}_{\mathrm{f}}^{\mathrm{T}} = \boldsymbol{R}_{\mathrm{C}}^{\mathrm{CDH}}\boldsymbol{\omega}_{\mathrm{f}}^{\mathrm{C}} \tag{14}$$

In the previous expressions, the matrix $\boldsymbol{R}_{\mathrm{C}}^{\mathrm{H}}$ is calculated with Eq. (6) using the final chaser attitude $\boldsymbol{\sigma}_{\mathrm{f}}^{\mathrm{C}}$. Similarly, $\boldsymbol{R}_{\mathrm{T}}^{\mathrm{H}}$ is calculated with Eq. (9) using $\boldsymbol{q}_{\mathrm{f}}^{\mathrm{T}}$.

B. Path Constraints

Proximity operations, with either cooperative or noncooperative targets, require the chaser spacecraft to follow safe and feasible trajectories until mechanical contact with the target spacecraft is achieved [22,27]. For this reason, the following constraints are imposed to the chaser trajectory.

Sensor field-of-view constraint: The chaser spacecraft is equipped with rendezvous sensors to detect the relative distance and attitude of the target spacecraft. To allow the pose estimation at any instant of time during the docking procedure, the chaser must maneuver in such a way to keep the target spacecraft always in the sensor field of view (FOV). As can be observed in Fig. 2, the rendezvous sensor is mounted along the axis of the chaser's docking interface, whereas the sensor FOV is defined by the boresight direction $\boldsymbol{b}^{\mathrm{C}}$ and by the half-cone angle α_{FOV}. The sensor FOV constraint can be expressed mathematically as

$$\left(-\boldsymbol{R}_{\mathrm{H}}^{\mathrm{C}}\begin{bmatrix} x \\ y \\ z \end{bmatrix} - \mathbf{s}_{\mathrm{C}}\right)\cdot\boldsymbol{b}^{\mathrm{C}} \geq \left\| -\boldsymbol{R}_{\mathrm{H}}^{\mathrm{C}}\begin{bmatrix} x \\ y \\ z \end{bmatrix} - \mathbf{s}_{\mathrm{C}}\right\| \cos(\alpha_{\mathrm{FOV}}) \tag{15}$$

where the vector $-(-\boldsymbol{R}_{\mathrm{H}}^{\mathrm{C}}[x \quad y \quad z]^{\mathrm{T}} - \mathbf{s}_{\mathrm{C}})$ is the position of the target center of mass with respect to the sensor expressed in the chaser principal coordinate system C. Therefore, Eq. (15) ensures that the angle defined by the sensor boresight direction and the vector $-(-\boldsymbol{R}_{\mathrm{H}}^{\mathrm{C}}[x \quad y \quad z]^{\mathrm{T}} - \mathbf{s}_{\mathrm{C}})$ remains lower than the maximum allowable angle α_{FOV}.

Collision avoidance: Any accidental collision between spacecraft must be avoided [15,22]. Consequently, the distance between the chaser docking point and the target surface must be larger than a minimum distance r_{safe}, which represents the radius of the "keep-out" zone [22]. This constraint can be expressed as

$$\left\| \begin{bmatrix} x \\ y \\ z \end{bmatrix} + \boldsymbol{R}_{\mathrm{C}}^{\mathrm{H}}\boldsymbol{l}^{\mathrm{C}} \right\| \geq r_{\mathrm{safe}} \tag{16}$$

Because of the constraint in Eq. (15), the chaser docking point is oriented toward the target spacecraft at any instant during the maneuver; moreover, it is the part of the chaser having the minimum

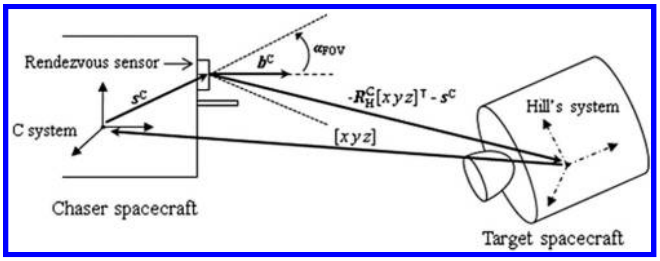

Fig. 2 Schematic representation of the sensor field-of-view constraint.

distance from the target surface (see also Fig. 2). By imposing the collision avoidance at the chaser docking point, we enforce this constraint to any other parts of the chaser spacecraft.

Handling controls upper and lower bounds: Because of design constraints, thrusters and reaction wheels have finite upper (and lower) bounds on the available force and torque. These constraints are enforced in terms of control components as

$$\boldsymbol{T}^{\mathrm{C}}_{\min} \leq \boldsymbol{T}^{\mathrm{C}} \leq \boldsymbol{T}^{\mathrm{C}}_{\max} \quad \boldsymbol{F}^{\mathrm{C}}_{\min} \leq \boldsymbol{F}^{\mathrm{C}} \leq \boldsymbol{F}^{\mathrm{C}}_{\max} \tag{17}$$

C. Optimal Control Problem Formulation

In this work, minimum energy maneuvers are considered; therefore, the performance index is defined as

$$J = \frac{1}{2}\int_0^{t_{\mathrm{f}}}\left(\left(\frac{F_x^{\mathrm{C}}}{m_{\mathrm{C}}}\right)^2 + \left(\frac{F_y^{\mathrm{C}}}{m_{\mathrm{C}}}\right)^2 + \left(\frac{F_z^{\mathrm{C}}}{m_{\mathrm{C}}}\right)^2 + \left(\frac{\mathrm{T}_x^{\mathrm{C}}}{L_{\mathrm{eq}} m_{\mathrm{C}}}\right)^2 + \left(\frac{\mathrm{T}_y^{C}}{L_{\mathrm{eq}} m_{C}}\right)^2 + \left(\frac{\mathrm{T}_z^{C}}{L_{\mathrm{eq}} m_{C}}\right)^2\right) \mathrm{d}t \tag{18}$$

In the previous equation, L_{eq} is a length parameter used to convert the control torque into an equivalent force. In this paper, we consider L_{eq} a given parameter related to the size of the chaser spacecraft. However, one may also consider L_{eq} a weighting factor between force and torque and, therefore, a varied parameter to be optimized. Notably in this paper, the optimization of the maneuver energy is chosen over the propellant mass because the resulting performance index function, in Eq. (18), has the properties of being continuous, quadratic, and differentiable. These aspects are indeed important for enabling rapid optimization using a nonlinear quadratic solver.

The optimal control problem for the docking maneuver can be stated as follows: find controls histories $\boldsymbol{T}^{\mathrm{C}}$ and $\boldsymbol{F}^{\mathrm{C}}$ that minimize J and, at the same time, transfer the system described by Eqs. (1–8) from an initial state

$$\boldsymbol{x}_0 = [x_0\ y_0\ z_0\ \dot{x}_0\ \dot{y}_0\ \dot{z}_0\ \omega^{\mathrm{C}}_{x_0}\ \omega^{\mathrm{C}}_{y_0}\ \omega^{\mathrm{C}}_{z_0}\ \sigma^{\mathrm{C}}_{1_0}\ \sigma^{\mathrm{C}}_{2_0}\ \sigma^{\mathrm{C}}_{3_0}\ \omega^{\mathrm{T}}_{x_0}\ \omega^{\mathrm{T}}_{y_0}\ \omega^{\mathrm{T}}_{z_0}\ q^{\mathrm{T}}_{1_0}\ q^{\mathrm{T}}_{2_0}\ q^{\mathrm{T}}_{3_0}\ q^{\mathrm{T}}_{4_0}]$$

to a final state

$$\boldsymbol{x}_{\mathrm{f}} = [x_{\mathrm{f}}\ y_{\mathrm{f}}\ z_{\mathrm{f}}\ \dot{x}_{\mathrm{f}}\ \dot{y}_{\mathrm{f}}\ \dot{z}_{\mathrm{f}}\ \omega^{\mathrm{C}}_{x_{\mathrm{f}}}\ \omega^{\mathrm{C}}_{y_{\mathrm{f}}}\ \omega^{\mathrm{C}}_{z_{\mathrm{f}}}\ \sigma^{\mathrm{C}}_{1_{\mathrm{f}}}\ \sigma^{\mathrm{C}}_{2_{\mathrm{f}}}\ \sigma^{\mathrm{C}}_{3_{\mathrm{f}}}\ \omega^{\mathrm{T}}_{x_{\mathrm{f}}}\ \omega^{\mathrm{T}}_{y_{\mathrm{f}}}\ \omega^{\mathrm{T}}_{z_{\mathrm{f}}}\ q^{\mathrm{T}}_{1_{\mathrm{f}}}\ q^{\mathrm{T}}_{2_{\mathrm{f}}}\ q^{\mathrm{T}}_{3_{\mathrm{f}}}\ q^{\mathrm{T}}_{4_{\mathrm{f}}}]$$

that satisfies Eqs. (11–14), while respecting the path constraints in Eqs. (15–17).

III. Open-Loop Trajectory Optimization Through the Inverse Dynamics Method

The guidance algorithm proposed in the following employs the inverse dynamics method for rapid suboptimal trajectory generation. In the inverse dynamics method, the optimal control problem is converted into an equivalent nonlinear programming problem by describing the chaser trajectory components with a set of interpolating functions defined in the time domain [25,28]. Some of the functions' polynomial coefficients will be linked to the boundary conditions on the trajectory, whereas other will be unconstrained and therefore become part of the varied parameters set of the resultant nonlinear programming problem. By inverting the dynamics, each state variable of the system dynamics model and each control component can be expressed as function of the parameterized trajectory and its derivatives. In particular, for the considered two-spacecraft rendezvous problem, it results in the following expressions:

$$\boldsymbol{\omega}^{\mathrm{C}}(t) = \boldsymbol{f}_1(\boldsymbol{\sigma}^{\mathrm{C}}, \dot{\boldsymbol{\sigma}}^{\mathrm{C}}), \boldsymbol{T}^{\mathrm{C}}(t) = \boldsymbol{f}_2(\boldsymbol{\sigma}^{\mathrm{C}}, \dot{\boldsymbol{\sigma}}^{\mathrm{C}}, \ddot{\boldsymbol{\sigma}}^{\mathrm{C}}),$$
$$\boldsymbol{F}^{\mathrm{H}}(t) = \boldsymbol{f}_3(x, y, z, \dot{x}, \dot{y}, \dot{z}, \ddot{x}, \ddot{y}, \ddot{z}) \tag{19}$$

In turn, also the performance index J of the nonlinear control problem can be expressed as function of the parameterized trajectory, and therefore, it can be minimized through the optimization of the varied parameters set composed by the unconstrained polynomial coefficients.

A. Parameterization of the Translational Trajectory

Following the inverse dynamics approach, the translational trajectory of the chaser spacecraft is represented by a set of functions defined in the time domain. Among all the possible parameterization functions (such as B-splines, Hermite polynomials, Bezier curves), we choose polynomials because they ensure a favorable tradeoff between computational speed in the optimization process and optimality [28]. Therefore, the trajectory of the chaser center of mass in the Hill coordinate system is represented by a set of polynomials of order n defined in the time domain

$$x(y) = \sum_{i=0}^{n} b_{1,i} t^i, \qquad y(t) = \sum_{i=0}^{n} b_{2,i} t^i, \qquad z(t) = \sum_{i=0}^{n} b_{3,i} t^i \tag{20}$$

which imply

$$\dot{x}(t) = \sum_{i=1}^{n} i b_{1,i} t^{i-1}, \quad \dot{y}(t) = \sum_{i=1}^{n} i b_{2,i} t^{i-1}, \quad \dot{z}(t) = \sum_{i=1}^{n} i b_{3,i} t^{i-1} \tag{21}$$

$$\ddot{x}(t) = \sum_{i=2}^{n} i(i-1) b_{1,i} t^{i-2}, \qquad \ddot{y}(t) = \sum_{i=2}^{n} i(i-1) b_{2,i} t^{i-2},$$
$$\ddot{z}(t) = \sum_{i=2}^{n} i(i-1) b_{3,i} t^{i-2} \tag{22}$$

As mentioned before, the certain polynomial coefficients $b_{1,i}$, $b_{2,i}$, and $b_{3,i}$ can be chosen in such a way that the boundary conditions on chaser position and velocity are systematically enforced. By imposing in Eqs. (20) and (21) the initial values x_0, y_0, z_0 and $\dot{x}_0$, $\dot{y}_0$, $\dot{z}_0$ at $t = 0$ s, we obtain the following expressions for the coefficients $b_{1,0}$, $b_{2,0}$, $b_{3,0}$, $b_{1,1}$, $b_{2,1}$, and $b_{3,1}$:

$$\begin{aligned} b_{1,0} &= x_0 \qquad & b_{2,0} &= y_0 \qquad & b_{3,0} &= z_0 \\ b_{1,1} &= \dot{x}_0 \qquad & b_{2,1} &= \dot{y}_0 \qquad & b_{3,1} &= \dot{z}_0 \end{aligned} \tag{23}$$

Similarly, the expressions of the coefficients $b_{1,n}$, $b_{2,n}$, $b_{3,n}$, $b_{1,n-1}$, $b_{2,n-1}$, and $b_{3,n-1}$ are obtained by imposing the final values x_{f}, y_{f}, z_{f} and $\dot{x}_{\mathrm{f}}$, $\dot{y}_{\mathrm{f}}$, $\dot{z}_{\mathrm{f}}$ in Eqs. (20) and (21) at $t = t_{\mathrm{f}}$. For the coefficients $b_{1,n}$ and $b_{1,n-1}$ of the x component, it results in

$$b_{1,n} = \frac{x_{\mathrm{f}} - \sum_{i=0}^{n-1} b_{1,i} t_{\mathrm{f}}^i}{t_{\mathrm{f}}^n},$$
$$b_{1,n-1} = \frac{\dot{x}_{\mathrm{f}} - \sum_{i=0}^{n-2} i b_{1,i} t_{\mathrm{f}}^{i-1} - n b_{1,n} t_{\mathrm{f}}^{i-1}}{(n-1) t_{\mathrm{f}}^{n-2}} \tag{24}$$

whereas analogous expressions are obtained for $b_{2,n}$, $b_{3,n}$, $b_{2,n-1}$, and $b_{3,n-1}$. Note that the initial conditions x_0, y_0, z_0 and $\dot{x}_0$, $\dot{y}_0$, $\dot{z}_0$ are directly provided by the estimation of the current chaser state. The final conditions x_{f}, y_{f}, z_{f} and $\dot{x}_{\mathrm{f}}$, $\dot{y}_{\mathrm{f}}$, $\dot{z}_{\mathrm{f}}$ are calculated from the final target state using Eqs. (11–14), where the final state of the system is estimated by propagating the dynamics Eqs. (1–8). This aspect will be discussed with more details in Sec. IV. As a consequence of this procedure, the polynomial coefficients $b_{j,0}$, $b_{j,1}$, $b_{j,n}$, and $b_{j,n-1}$ $(j = 1, 2, 3)$ are determined, whereas the rest of the coefficients are varied parameters to be optimized. To allow the optimization of the trajectory, the order of each polynomial must satisfy the equation

$$n \geq n_B \tag{25}$$

where n_B is the number of boundary conditions imposed to a single trajectory component (by imposing end-point position and velocity, it results in $n_B = 4$). In this way, at least one polynomial coefficient for each trajectory component is a varied parameter to be optimized, allowing flexibility on the shape of the trajectory. The higher the order n is, the higher the number of varied parameters is. On the other hand, to avoid Runge's phenomena (oscillations at the edges of the time interval) typical of high-order polynomials, the polynomial order must be limited to $n \leq 8$ [29].

By inverting Eq. (1), it yields to the following expression of the control thrusts expressed in the Hill coordinate system:

$$\begin{aligned} F_x^{\mathrm{H}} &= m_{\mathrm{C}}(\ddot{x} - 2\Omega\dot{y} - 3\Omega^2 x) \\ F_y^{\mathrm{H}} &= m_{\mathrm{C}}(\ddot{y} + 2\Omega\dot{x}) \\ F_z^{\mathrm{H}} &= m_{\mathrm{C}}(\ddot{z} + \Omega^2 z) \end{aligned} \tag{26}$$

The procedure provides analytical expressions in the time domain of translational velocities, accelerations, and control thrusts. In particular, the expressions of the controls are in the following form:

$$\begin{aligned} &F_j^{\mathrm{H}} = F_j^{\mathrm{H}}(x_0, \dot{x}_0, x_{\mathrm{f}}, \dot{x}_{\mathrm{f}} y_0, \dot{y}_0, y_{\mathrm{f}}, \dot{y}_{\mathrm{f}}, b_{1,2}, b_{2,2}, \ldots, b_{1,n-2}, b_{2,n-2}, m_{\mathrm{C}}, \Omega, t_{\mathrm{f}}, t), \\ &j = x, y \\ &F_z^{\mathrm{H}} = F_z^{\mathrm{H}}(z_0, \dot{z}_0, z_{\mathrm{f}}, \dot{z}_{\mathrm{f}}, b_{3,2}, \ldots, b_{3,n-2}, m_{\mathrm{C}}, \Omega, t_{\mathrm{f}}, t), \quad t \in [0, t_{\mathrm{f}}] \end{aligned} \tag{27}$$

These expressions involve a set of given parameters x_0, $\dot{x}_0$, y_0, $\dot{y}_0$, z_0, $\dot{z}_0$, x_{f}, $\dot{x}_{\mathrm{f}}$, y_{f}, $\dot{y}_{\mathrm{f}}$, z_{f}, $\dot{z}_{\mathrm{f}}$, m_{C}, Ω, and t_{f} and a set of varied parameters $b_{1,2}, b_{2,2}, b_{3,2}, \ldots, b_{1,n-2}, b_{2,n-2}$, and $b_{3,n-2}$ to be optimized.

B. Parameterization of the Attitude Trajectory

Regarding the attitude trajectory of the chaser spacecraft, we proceed similarly to the procedure described for the translation; namely, the attitude trajectory of the chaser principal coordinate system C with respect to the Hill system in terms of MRP is represented with a set of polynomials in the time domain:

$$\sigma_j^{\mathrm{C}}(t) = \sum_{i=0}^{n} a_{j,i} t^i \qquad j = 1, 2, 3 \tag{28}$$

Accordingly, the time derivatives of the trajectory components are given by

$$\dot{\sigma}_j^{\mathrm{C}}(t) = \sum_{i=1}^{n} i a_{j,i} t^{i-1}, \qquad j = 1, 2, 3 \tag{29}$$

$$\ddot{\sigma}_j^{\mathrm{C}}(t) = \sum_{i=2}^{n} i(i-1) a_{j,i} t^{i-2} \qquad j = 1, 2, 3 \tag{30}$$

Also, in this case, the polynomial coefficients $a_{j,i}$ can be obtained by imposing the boundary conditions $\boldsymbol{\sigma}_0^{\mathrm{C}}, \dot{\boldsymbol{\sigma}}_0^{\mathrm{C}}, \boldsymbol{\sigma}_{\mathrm{f}}^{\mathrm{C}}$, and $\dot{\boldsymbol{\sigma}}_{\mathrm{f}}^{\mathrm{C}}$ to Eqs. (28) and (29). The expressions for the coefficients $a_{j,0}$, $a_{j,1}$, $a_{j,n}$, and $a_{j,n-1}$ are given by

$$a_{j,0} = \sigma_{j0}^{\mathrm{C}}, \qquad a_{j,1} = \dot{\sigma}_{j0}^{\mathrm{C}}, \qquad j = 1, 2, 3 \tag{31}$$

$$\begin{aligned} a_{j,n} &= \frac{\sigma_{j_{\mathrm{f}}}^{C} - \sum_{i=0}^{n-1} a_{j,i} t_{\mathrm{f}}^{i}}{t_{\mathrm{f}}^{n}}, \\ a_{j,n-1} &= \frac{\dot{\sigma}_{j_{\mathrm{f}}}^{\mathrm{C}} - \sum_{i=0}^{n-2} i a_{j,i} t_{\mathrm{f}}^{i-1} - n a_{j,n} t_{\mathrm{f}}^{i-1}}{(n-1) t_{\mathrm{f}}^{n-2}}, \qquad j = 1, 2, 3 \end{aligned} \tag{32}$$

By inverting Eq. (4), we obtain the following expression of the angular velocity ${}^{\mathrm{H}}\boldsymbol{\omega}^{\mathrm{C}}$:

$${}^{\mathrm{H}}\boldsymbol{\omega}^{\mathrm{C}} = 4\boldsymbol{B}(\boldsymbol{\sigma}^{\mathrm{C}})^{-1} \dot{\boldsymbol{\sigma}}^{\mathrm{C}} \tag{33}$$

where the inverse of the matrix $\boldsymbol{B}(\boldsymbol{\sigma}^{\mathrm{C}})$ is given by [26]

$$\boldsymbol{B}(\boldsymbol{\sigma}^{\mathrm{C}})^{-1} = \frac{1}{(1 + \|\boldsymbol{\sigma}^{\mathrm{C}}\|^2)^2} \boldsymbol{B}(\boldsymbol{\sigma}^{\mathrm{C}})^{\top}$$

The time derivative of Eq. (33) provides the expressions of the angular acceleration with respect to the Hill coordinate system [25,26]:

$${}^{\mathrm{H}}\dot{\boldsymbol{\omega}}^{\mathrm{C}} = \frac{1}{(1 + \|\boldsymbol{\sigma}^{\mathrm{C}}\|^2)^2} \boldsymbol{B}(\boldsymbol{\sigma}^{\mathrm{C}})^{\top} [4\ddot{\boldsymbol{\sigma}}^{\mathrm{C}} - \dot{\boldsymbol{B}}(\boldsymbol{\sigma}^{\mathrm{C}}) {}^{\mathrm{H}}\boldsymbol{\omega}^{\mathrm{C}}] \tag{34}$$

The expressions of the control torques are finally obtained by inverting the dynamics expressed in Eq. (2):

$$\begin{aligned} \mathrm{T}_x^{\mathrm{C}} &= I_{xx}^{\mathrm{C}} \dot{\omega}_x^{\mathrm{C}} + (I_{zz}^{\mathrm{C}} - I_{yy}^{\mathrm{C}}) \omega_z^{\mathrm{C}} \omega_y^{\mathrm{C}} \\ \mathrm{T}_y^{\mathrm{C}} &= I_{yy}^{\mathrm{C}} \dot{\omega}_y^{\mathrm{C}} + (I_{xx}^{\mathrm{C}} - I_{zz}^{\mathrm{C}}) \omega_z^{\mathrm{C}} \omega_x^{\mathrm{C}} \\ \mathrm{T}_z^{\mathrm{C}} &= I_{zz}^{\mathrm{C}} \dot{\omega}_z^{\mathrm{C}} + (I_{yy}^{\mathrm{C}} - I_{xx}^{\mathrm{C}}) \omega_x^{\mathrm{C}} \omega_y^{\mathrm{C}} \end{aligned} \tag{35}$$

where the components of $\boldsymbol{\omega}^{\mathrm{C}}$ are obtained from Eq. (5) by inserting the expression of ${}^{\mathrm{H}}\boldsymbol{\omega}^{\mathrm{C}}$. Similarly, the components of $\dot{\boldsymbol{\omega}}^{\mathrm{C}}$, which represent the angular acceleration vector with respect to the ECI coordinate system, are obtained from ${}^{\mathrm{H}}\dot{\boldsymbol{\omega}}^{\mathrm{C}}$ using the time derivative of Eq. (5):

$$\begin{bmatrix} \dot{\omega}_x^{\mathrm{C}} \\ \dot{\omega}_y^{\mathrm{C}} \\ \dot{\omega}_z^{\mathrm{C}} \end{bmatrix} = \begin{bmatrix} {}^{\mathrm{H}}\dot{\omega}_x^{\mathrm{C}} \\ {}^{\mathrm{H}}\dot{\omega}_y^{\mathrm{C}} \\ {}^{\mathrm{H}}\dot{\omega}_z^{\mathrm{C}} \end{bmatrix} + \dot{\boldsymbol{R}}_{\mathrm{H}}^{\mathrm{C}} \begin{bmatrix} 0 \\ 0 \\ \Omega \end{bmatrix} \tag{36}$$

This procedure allows to obtain analytical expressions in the time domain of angular velocities, accelerations, and control torques. In particular, the expressions of the control torques are in the following form:

$$\begin{aligned} &\mathrm{T}_j^{\mathrm{C}} = \mathrm{T}_j^{\mathrm{C}}(\boldsymbol{\sigma}_0^{\mathrm{C}}, \dot{\boldsymbol{\sigma}}_0^{\mathrm{C}}, \boldsymbol{\sigma}_{\mathrm{f}}^{\mathrm{C}}, \dot{\boldsymbol{\sigma}}_{\mathrm{f}}^{\mathrm{C}}, a_{1,2}, a_{2,2}, a_{3,2}, \ldots, a_{1,n-2}, a_{2,n-2}, a_{3,n-2}, \\ &I_{xx}^{\mathrm{C}}, I_{yy}^{\mathrm{C}}, I_{zz}^{\mathrm{C}}, \Omega, t_{\mathrm{f}}, t), \qquad t \in [0, t_{\mathrm{f}}], \qquad j = x, y, z \end{aligned} \tag{37}$$

In these expressions, $\boldsymbol{\sigma}_0^{\mathrm{C}}$, $\dot{\boldsymbol{\sigma}}_0^{\mathrm{C}}$, $\boldsymbol{\sigma}_{\mathrm{f}}^{\mathrm{C}}$, $\dot{\boldsymbol{\sigma}}_{\mathrm{f}}^{\mathrm{C}}$, Ω, I_{xx}^{C}, I_{yy}^{C}, I_{zz}^{C}, and t_{f} are known parameters, whereas $a_{1,2}, a_{2,2}, a_{3,2}, \ldots, a_{1,n-2}, a_{2,n-2}$, and $a_{3,n-2}$ are the varied parameters.

C. Trajectory Optimization

At this point, the time domain $[0; t_{\mathrm{f}}]$ is discretized into N intervals, with $N + 1$ equidistant temporal nodes, and the performance index of the optimal control problem in Eq. (18) is integrated numerically using the expressions of the controls in Eqs. (26) and (35). This procedure allows to transform J into a (nonlinear) function of the given parameters and the varied parameters:

$$\begin{aligned} &J = J(\boldsymbol{\sigma}_0^{\mathrm{C}}, \dot{\boldsymbol{\sigma}}_0^{\mathrm{C}}, \boldsymbol{\sigma}_{\mathrm{f}}^{\mathrm{C}}, \dot{\boldsymbol{\sigma}}_{\mathrm{f}}^{\mathrm{C}}, x_0, \dot{x}_0, x_{\mathrm{f}}, \dot{x}_{\mathrm{f}} y_0, \dot{y}_0, y_{\mathrm{f}}, \dot{y}_{\mathrm{f}}, z_0, \dot{z}_0, z_{\mathrm{f}}, \dot{z}_{\mathrm{f}}, a_{j,2}, \\ &b_{j,2}, \ldots, a_{j,n-2}, b_{j,n-2}, m_{\mathrm{C}}, I_{xx}^{\mathrm{C}}, I_{yy}^{\mathrm{C}}, I_{zz}^{\mathrm{C}}, \Omega, t_{\mathrm{f}}), \qquad j = 1, 2, 3 \end{aligned} \tag{38}$$

Consequently, the initial optimal control problem is converted into the following equivalent nonlinear programming problem. Given the set of known parameters $x_0, \dot{x}_0, y_0, \dot{y}_0, z_0, \dot{z}_0, x_f, \dot{x}_f, y_f, \dot{y}_f, z_f, \dot{z}_f, m_C$, $\boldsymbol{\sigma}_0^C, \dot{\boldsymbol{\sigma}}_0^C, \boldsymbol{\sigma}_f^C, \dot{\boldsymbol{\sigma}}_f^C, \Omega, I_{xx}^C, I_{yy}^C, I_{zz}^C$ and, t_f, minimize the function J in Eq. (38) with respect to the varied parameters $a_{1,2}$, $a_{2,2}$, $a_{3,2}$, $b_{1,2}, b_{2,2}, b_{3,2}, \ldots, b_{2,n-2}, b_{3,n-2}$, subjected to the constraint Eqs. (15–17) evaluated at each temporal node.

It is important to note that the constraints are enforced at finite number of points, being the temporal nodes. In addition, the discrete approximation of the continuous function J in Eq. (18) depends on the choice of the integration technique along with the number of temporal nodes.

This constrained optimization problem is solved using SNOPT, which employs a sequential quadratic programming algorithm to optimize the varied parameters of the problem [30]. This solver has been selected because it is able to solve efficiently problems with a limited number of varied parameters and gradients of the constraints difficult to evaluate [31].

Before starting the optimization process, Eqs. (3) and (8) are integrated, and the constraint Eqs. (11–14) are then applied to calculate the chaser's final state, required to impose the end-point conditions of the trajectory. Note that the maneuver duration t_f is assumed to be a fixed parameter of the optimization problem, and it is estimated using the algorithm described in the Appendix. This choice is driven by the need to further decrease the computational speed required by the solver to converge to an optimal solution [25]. Conversely, leaving the maneuver duration as varied parameter requires the determination of the final state at every iteration of the solver, which reflects in lower computational speed.

IV. Guidance Algorithm

The proposed guidance algorithm is based on the closed-loop implementation of the trajectory optimization algorithm described in the previous section. During the maneuver, a new docking trajectory is recomputed at a certain frequency (depending on the computational time required to solve the optimization problem) using the latest update of the system state vector. In this way, the docking trajectory is repeatedly adjusted based on the current state of both chaser and target. In addition, a control actuation system commands the controls generated by the guidance into the dynamics system at a sampling rate of $t_{\min}$ for both position and attitude.

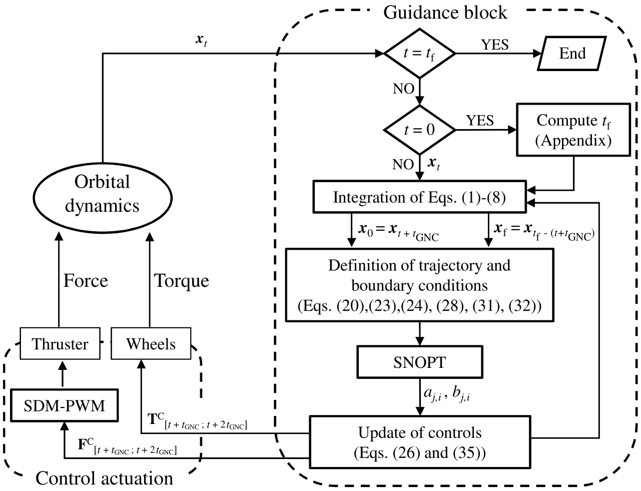
Guidance block
x_t
$t = t_f$
YES
End
NO
$t = 0$
YES
Compute t_f (Appendix)
NO
x_t
Orbital dynamics
Integration of Eqs. (1)-(8)
$x_0 = x_{t+t_{GNC}}$
$x_f = x_{t_f-(t+t_{GNC})}$
Definition of trajectory and boundary conditions (Eqs. (20),(23),(24), (28), (31), (32))
Force
Torque
Thruster
Wheels
SNOPT
$a_{j,i}, b_{j,i}$
SDM-PWM
$\mathbf{T}^C_{[t+t_{GNC}\,;\,t+2t_{GNC}]}$
$\mathbf{F}^C_{[t+t_{GNC}\,;\,t+2t_{GNC}]}$
Update of controls (Eqs. (26) and (35))
Control actuation

Fig. 3 Block diagram of the guidance system.

Figure 3 represents the block diagram of such guidance algorithm. The current state vector $\boldsymbol{x}_t$, corresponding to the particular instant of time t of the maneuver and assumed to be available from the navigation system, is updated at a certain frequency and fed to the guidance block. In it, a new near-optimal trajectory is recomputed with the inverse dynamics approach. The output of the guidance block consists of the refreshed values of near-optimal controls $\boldsymbol{F}^C$ and $\boldsymbol{T}^C$ for the remaining duration of the maneuver, which have smooth histories, owing to the nature of the inverse dynamics method [25]. To be actuated, these controls are fed to the actuation block, as shown in Fig. 3. The low-level attitude controller samples the torque history $\boldsymbol{T}^C$ at a rate of $t_{\min}$ and commands it using the reaction wheels. On the contrary, the continuous force history $\boldsymbol{F}^C$ is first converted into equivalent sequences of on–off pulses and then sampled by the low-level position controller at a rate of $t_{\min}$. Control forces are finally actuated by cold-gas thrusters. This entire process is repeated until maneuver completion. Notably, in the first execution of the loop, the maneuver duration t_f is computed in the guidance block before the trajectory optimization using the algorithm described in the Appendix.

The main constraint of this closed-loop implementation is that the execution frequency must be chosen such to ensure SNOPT to converge to an optimal solution for every loop execution. In fact, the period of the loop execution must be higher than the maximum expected computational time required by SNOPT, which can be estimated by analyzing the performance of the trajectory optimization algorithm (in open-loop).

Because of the fact that SNOPT is an iterative solver, there is no guarantee that an optimal solution will be always found within a certain computational time. Therefore, it is necessary to ensure that the guidance block always provides the output controls for every loop execution. This is done by considering the following precautions.

Limiting the number of iterations: The number of maximum iterations is limited to ensure that SNOPT provides a suboptimal solution within the available time t_{GNC} (note that a safety margin should be considered). The computational time required by SNOPT to execute a single iteration can be estimated by analyzing the performance of the trajectory optimization algorithm in open-loop. Then, the maximum number of iterations within t_{GNC} is calculated.

Using previous solution of the nonlinear programming problem: One of the advantages of the inverse dynamics approach is that the controls are determined by the polynomial coefficients along with the chaser end-point conditions. Therefore, if unexpected problems are encountered by SNOPT, the controls are determined using the polynomial coefficients from the previous trajectory optimization.

A. Guidance Block

As shown in Fig. 3, the guidance block reformulates the optimal control problem at each loop execution. Starting from the most current update of the state vector $\boldsymbol{x}_t$, the rendezvous dynamics described by Eqs. (1–8) is propagated in time for the remaining maneuver duration $t_f - (t + t_{GNC})$ to determine the new initial state vector $\boldsymbol{x}_{t+t_{GNC}}$ and the new final state vector $\boldsymbol{x}_{t_f-(t+t_{GNC})}$ for the new trajectory generation. In particular, the initial state vector for the new trajectory optimization corresponds to the time $t + t_{GNC}$ because the updated controls will be commanded at the end of the current loop

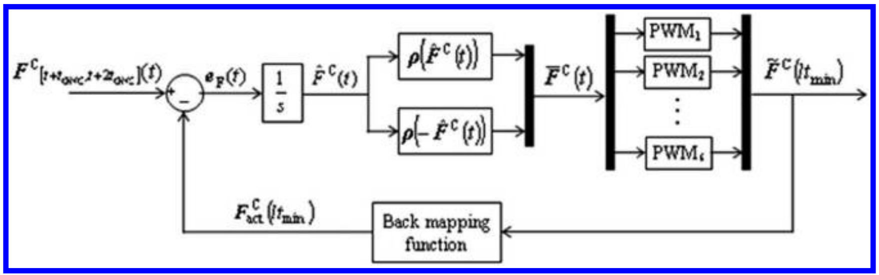

Fig. 4 SDM-PWM actuation schematic.

iteration. Furthermore, although the maneuver duration t_f is a fixed parameter, the final state vector is updated in every loop execution based on the latest current system state. This procedure increases flexibility of the guidance algorithm and robustness to noise in the initial state vector.

Once the end-point conditions are estimated, the trajectory is parameterized using Eqs. (20), (23), (24), (28), (31), and (32). Finally, optimal polynomial coefficients computed by SNOPT are used to update the time histories of the controls, which will be commanded with the control actuation block and actuated through the chaser thrusters and reaction wheels.

B. Control Actuation

As mentioned before, the chaser attitude is controlled by a set of three reaction wheels; therefore, the low-level attitude controller samples the time history of the torque $\boldsymbol{T}^{\mathrm{C}}[t + t_{\mathrm{GNC}}; t + 2t_{\mathrm{GNC}}]$ and commands it at a rate of $t_{\min}$. Conversely, the chaser translation capability is assumed to be featured by six cold-gas thrusters, with three of them aligned along the positive semi-axis of the principal coordinate system C and the other three directed in the opposite directions. Each thruster is assumed to produce only on–off thrust states, i.e., either zero or maximum thrust (bang–bang control). In this configuration, the three components of the thrust control history $\boldsymbol{F}^{\mathrm{C}}[t + t_{\mathrm{GNC}}; t + 2t_{\mathrm{GNC}}]$ must be converted into six sequences of on–off pulses, components of the actuated thrust vector $\tilde{\boldsymbol{F}}^{\mathrm{C}}(lt_{\min}) = [F_1^{\mathrm{C}}(lt_{\min}), F_2^{\mathrm{C}}(lt_{\min}), \ldots, F_6^{\mathrm{C}}(lt_{\min})]^{\mathrm{T}} \quad l \in [0, 1, 2, \ldots, L]$, with $L = \mathrm{integer}(t_{\mathrm{GNC}}/t_{\min})$ the number of intervals in the guidance period t_{GNC}.

This analog-to-digital conversion process is performed by the sigma-delta modulation combined with the pulse-width modulation (SDM-PWM technique) [32,33], as shown in Fig. 4. In particular, this technique is executed after the guidance block to convert the history $\boldsymbol{F}^{\mathrm{C}}[t + t_{\mathrm{GNC}}; t + 2t_{\mathrm{GNC}}]$ into an equivalent sequences of maximum-thrust pulses, which is sampled by the low-level position controller and actuated by the thrusters.

The basic principle of the SDM-PWM consists of measuring the integral $\hat{\boldsymbol{F}}^{\mathrm{C}}(t) \in \boldsymbol{R}^{3x1}$ of the actuation error $\boldsymbol{e}_F(t) \in \boldsymbol{R}^{3x1}$; namely, the difference between the input analog thrust $\boldsymbol{F}^{\mathrm{C}}$ and the actuated thrust $\boldsymbol{F}^{\mathrm{C}}_{\mathrm{act}}$. Such integral is then mapped into an equivalent vector $\bar{\boldsymbol{F}}^{\mathrm{C}}(t) \in \boldsymbol{R}^{6x1}$ characterized by six nonnegative continuous components. Each of these is then converted into sequences of on–off pulses using a PWM [34]. It is important to note that the components of $\hat{\boldsymbol{F}}^{\mathrm{C}}$ are three real numbers (which can attain negative values), whereas the six thrusters of the chaser spacecraft can actuate nonnegative values of thrust. This requires the following mapping process to convert these three components into six equivalent nonnegative components of the vector $\bar{\boldsymbol{F}}^{\mathrm{C}}$:

$$\bar{\boldsymbol{F}}^{\mathrm{C}} = \begin{bmatrix} \boldsymbol{\rho}(\hat{\boldsymbol{F}}^{\mathrm{C}}) \\ \boldsymbol{\rho}(-\hat{\boldsymbol{F}}^{\mathrm{C}}) \end{bmatrix} \tag{39}$$

with $\boldsymbol{\rho}$: $\boldsymbol{R}^3 \to \boldsymbol{R}^3$ the ramp function, defined as

$$\rho_i(\hat{F}_i^{\mathrm{C}}) = \begin{cases} \hat{F}_i^{\mathrm{C}} & \text{if } \hat{F}_i^{\mathrm{C}} \geq 0 \\ 0 & \text{if } \hat{F}_i^{\mathrm{C}} < 0 \end{cases} \qquad i = 1, 2, 3 \tag{40}$$

Because of this analog-to-digital conversion process, the actuated thrust slightly differs from the requested thrust. In particular, from Eqs. (39) and (40), we have the following back mapping function:

$$\boldsymbol{F}^{\mathrm{C}}_{\mathrm{act}}(lt_{\min}) = \begin{bmatrix} \tilde{F}_1(lt_{\min}) - \tilde{F}_4(lt_{\min}) \\ \tilde{F}_2(lt_{\min}) - \tilde{F}_5(lt_{\min}) \\ \tilde{F}_3(lt_{\min}) - \tilde{F}_6(lt_{\min}) \end{bmatrix} \tag{41}$$

V. Numerical Results

The numerical performance results in terms of optimality, robustness, and sensitivity to system noise of the proposed control system for docking maneuvers are presented in this section.

The docking maneuvers between an actuated chaser spacecraft and a noncooperative tumbling target spacecraft are considered for the numerical experiments. Tables 1 and 2 list the characteristics of the two spacecraft. Data of the chaser are taken from the servicer of the DEOS mission [35], whereas data of the target are taken from Envisat [36,37]. The safety radius r_{safe} that defines the keep-out zone in Eq. (16) is set to 4.60 m according to the position of the target docking port (Table 2). The chaser docking point must enter into the target docking interface with a relative translational speed $\|\boldsymbol{v}_{\mathrm{con}}\|$ of 0.01 m/s along the docking axis [4]. The shortest on-time of the chaser's cold-gas thrusters is 0.01 s.

The algorithm described in this paper has been implemented in Matlab Simulink environment [38] on a laptop with an Intel Core i7 U 2.8 GHz and 8.0 GB of RAM. The Simulink model for the orbital dynamics consists of the translational and rotational motions of each spacecraft with respect to the ECI system. The two spacecraft are assumed rigid bodies. The translational motion the center of mass is described by the two-body differential equation in Cowell's formulation [39]:

$$\ddot{\boldsymbol{r}} = -\frac{\mu}{\|\boldsymbol{r}\|^3}\boldsymbol{r} + \boldsymbol{a}_{\mathrm{ext}} \tag{42}$$

where $\boldsymbol{a}_{\mathrm{ext}}$ is the total external force vector acting on the spacecraft, and μ is the standard gravitational parameter of the Earth. The dynamics of the rotational motion of each spacecraft is represented by Euler's equation:

$$\boldsymbol{I}\dot{\boldsymbol{\omega}} + \boldsymbol{\omega} \times \boldsymbol{I}\boldsymbol{\omega} = \boldsymbol{T}_{\mathrm{ext}} \tag{43}$$

where $\boldsymbol{I}$ denotes the principal inertial tensor, and $\boldsymbol{T}_{\mathrm{ext}}$ is the external torque vector. The attitude of the spacecraft principal axes with respect to the ECI system is provided by Eq. (8) applied to the angular velocity vector $\boldsymbol{\omega}$ obtained from Eq. (43). The orbital dynamics model is solved in Simulink using a fourth-order Runge–Kutta method applied with a fixed time step of 0.01 s [39]. The current state vector $\boldsymbol{x}$ of the two-spacecraft rendezvous model is computed from the solutions of Eqs. (42) and (43).

The trajectory optimization algorithm of the control system employs fifth-order polynomials to represent the MRP of the chaser spacecraft attitude trajectory [25]. The same representation is used for each component of the translational trajectory. Because boundary

Table 1 Chaser spacecraft characteristics

Parameter	Value
I^{C}_{xx}, I^{C}_{yy}, I^{C}_{zz}, kg · m^2	2014, 1897, 1357
m_{C}, kg	961
Dimensions (body), m	3.10 × 2.0 × 1.80
$\boldsymbol{l}^{\mathrm{C}}$, m	[0 0 2.0]
$\boldsymbol{s}^{\mathrm{C}}$, m	[0 0 2.0]
$\boldsymbol{R}^{\mathrm{C}}_{\mathrm{CD}}$	[0 −1 0; 1 0 0; 0 0 1]
$\boldsymbol{b}^{\mathrm{C}}$	[001]
$F^{\mathrm{C}}_{j,\max}$, $F^{\mathrm{C}}_{j,\min}$, N	8, −8
$T^{\mathrm{C}}_{j,\max}$, $T^{\mathrm{C}}_{j,\min}$, N · m	10, −10
$t_{\min}$, s	0.01
α_{FOV}, deg	25

Table 2 Target spacecraft characteristics

Parameter	Value
I^{T}_{xx}, I^{T}_{yy}, I^{T}_{zz}, kg · m^2	17,023; 124,825; 129,112
Mass, kg	7828
Dimensions (body), m	9.20 × 2.6 × 2.6
Dimensions (solar array), m	15.00 × 2.00 × 0.03
$\boldsymbol{l}^{\mathrm{T}}$, m	[0 −4.60 0]
$\boldsymbol{R}^{\mathrm{T}}_{\mathrm{TD}}$	[1 0 0; 0 0 1; 0 −1 0]
Orbit altitude (eccentricity), km	773 (0)
Orbit inclination, deg	98.4

conditions on position and velocity (attitude and angular velocity for the rotation) are enforced through Eqs. (23), (24), (31), and (32), two varied parameters are optimized for each trajectory component. The reference length L_{eq} in Eq. (18) is 1.5 m, which corresponds to the average distance from the chaser center of mass and the reaction wheels position. The number of intervals that discretize the remaining maneuver time is $N = 24$ in every guidance cycle (see Sec. III.C). The constrained optimization problem generated with the inverse dynamics method is solved using SNOPT 7.2 [30] with an accuracy of 1e-7. Equations (1–8) are integrated in the guidance block (see Fig. 3) with a fourth-order Runge–Kutta method and a fixed time step of 0.2 s.

For the first trajectory optimization (first execution of the guidance block), the initial guess on the polynomial coefficients to be optimized is calculated using Eqs. (22) and (30) after imposing zero controls at the end points. Because two varied parameters are defined for each trajectory component, initial and final values of controls (thrust and torque) are enough to specify the initial guess. Successive optimizations use the previous optimal polynomial coefficients as new initial guess. In our experimental campaign, we have tested the trajectory optimization performed by SNOPT in open loop, recording peaks of computational time of about 8.0 s. Consequently, in the numerical experiments, the guidance algorithm has been executed at a rate of 0.1 Hz ($t_{\mathrm{GNC}} = 10$ s) to ensure a safety margin. Because SNOPT requires about 5 ms to execute a single internal iteration, the maximum number of iterations is set to 1800 to ensure a result within 10 s.

This section reports the results of three different analyses. The first analysis in Sec. V.A investigates the performance of the guidance algorithm in terms of docking precision, optimality of the trajectories, enforcement of the path constraints, and computational time required by SNOPT. In particular, this part focuses on evaluating the performance of the trajectory generation algorithm in the ideal case of perfect knowledge of current state vector and target inertia. Section V. B discusses the robustness of the guidance scheme, shown in Fig. 3, to various maneuvering situations. In this study, the control actuation includes the DSM-PWM (analog-to-digital) conversion of the thrust components for realistic control actuation. The algorithm is tested on 500 randomly chosen scenarios in the ideal case of perfect knowledge of the target. The third type of analysis is the sensitivity study to orbital perturbations in LEO (Sec. V.C) and to disturbances in the input state vector and in the target inertia (Sec. V.D). Notably, this study is essential to verify applicability of the guidance system to noncooperative maneuvers because the target inertia and relative state might be subjected to significant uncertainties.

A. Optimality, Computational Speed, and Constraints Verification

Three reference scenarios summarized in Table 3 are considered to analyze the docking accuracy and optimality of the trajectories generated by the guidance algorithm, verify the satisfaction of the path constraints, and evaluate the computational time required by SNOPT to solve the nonlinear programming problem of Sec. III.C. The maneuvers are R-bar approaches from identical initial conditions for both chaser and target but differ in the rotational motion of the target spacecraft. The angular rates of the target are taken from the estimated measurements of Envisat [36,40].

Table 3 Initial states of the target and chaser spacecraft for scenarios 1–3

Parameter	Value
x_0, y_0, z_0, m	–50, –11, 7
$\dot{x}_0$, $\dot{y}_0$, $\dot{z}_0$, m/s	0, 0, 0
$\boldsymbol{\omega}_0^{\mathrm{C}}$, deg /s	[000]
$\boldsymbol{\sigma}_0^{\mathrm{C}}$	[0.34 0.41 0.37]
$\boldsymbol{\omega}_0^{\mathrm{T}}$ (scenario 1), deg /s	[3.5 0.5 0.5]
$\boldsymbol{\omega}_0^{\mathrm{T}}$ (scenario 2), deg /s	[0.5 3.5 0.5]
$\boldsymbol{\omega}_0^{\mathrm{T}}$ (scenario 3), deg /s	[0.5 0.5 3.5]
$\boldsymbol{q}_0^{\mathrm{T}}$	[–0.5 –0.5 –0.5 0.5]

For the numerical experiments presented in this section, the analog-to-digital conversion process of the thrust components described in Sec. IV.B is bypassed, and the continuous controls generated by the inverse dynamics are directly injected into the dynamics model to analyze the performance of the guidance algorithm alone. We also assume perfect knowledge of the target state and inertia. The optimality of the resulting maneuvers is evaluated by comparison with reference optimal trajectories obtained by solving the optimal control problem posted in Sec. II with GPOPS II v1.0 [41]. For each scenario, GPOPS is executed 10 times using different initial guesses, generated by randomly perturbing the initial guess on the controls used for the cold start of the guidance system and the final state achieved with the maneuver (first guess on the final condition). The chosen reference optimal trajectory corresponds to the one having the minimum performance index. In this way, we avoid possible local minima of the reference solution. The accuracy of GPOPS has been set to 1e-7 for this analysis. Each optimization with GPOPS required between 20 and 60 min according to the first guess.

Table 4 summarizes the maneuver durations calculated with the algorithm in the Appendix as well as the relative states between the target spacecraft docking point and the chaser spacecraft docking point achieved at the end of the maneuvers. The relative states listed in the table are calculated using Eqs. (11–14). Axial and radial directions are intended with respect to the target spacecraft docking axis. Notably, the guidance algorithm allows reaching all the docking conditions in Eqs. (11–14) with high precision at the end of each maneuver. Furthermore, the algorithm for estimating the maneuver duration is capable to calculate feasible maneuver time durations.

Figure 5 illustrates the enforcement of the path constraints by the guidance during the maneuvers execution. The time history of the distance between the chaser spacecraft docking point and the keep-out zone is evaluated with Eq. (16), and it is represented in Fig. 5a. The minimum distance is 0 m in all the maneuvers and occurs at the mechanical contact between docking points. The time history of the angular distance from the chaser spacecraft rendezvous sensor boresight to the target spacecraft center of mass is calculated with Eq. (15), and it is shown in Fig. 5b. Also, in this case, the guidance imposes accurately the constraint. The achieved maximum angular distance is 25.02 deg during scenario 3.

Figure 6 represents the evolution of the computational time required by SNOPT to converge to a solution for each cycle (cycle duration $t_{\mathrm{GNC}} = 10$ s). In all the considered scenarios, higher computational times arise during the initial trajectory optimizations (within 15 calls of SNOPT), whereas lower computational times, with an average of 0.4 s, are observed in the second part of the maneuvers. Such behaviour can be explained by considering that SNOPT enforces the path and control constraints in new temporal nodes at each call, and the resulting trajectories progressively converge to the suboptimal solution of the constrained optimization problem. For this reason, SNOPT requires more iterations to converge in the initial calls, resulting in higher computational time. In the second part of the maneuver, SNOPT only updates the computed feasible trajectory because the constraints are imposed accurately enough, resulting in a faster convergence speed.

Figure 7 shows the evolution of the polynomial coefficients computed by SNOPT for scenario 1. As previously discussed, after the first dozen calls of SNOPT, the coefficients $a_{j,3}$ and $b_{j,3}$ stabilize to quasi-steady values. In the second part of the maneuver, only the coefficients $a_{j,2}$ and $b_{j,2}$ keep changing because these parameters are related to the new initial acceleration components according the following:

Table 4 Achieved docking conditions for scenarios 1–3

		Δr, m		Δv, m/s			
Scenario	t_{f}, s	Axial	Radial	Axial	Radial	$\Delta\theta_{\max}$, deg	$\Delta\omega_{\max}$, deg /s
1	410	2.4e-4	1.2e-4	1.0e-2	2.0e-5	5.7e-3	2.9e-4
2	310	–5.5e-4	1.8e-4	1.0e-2	2.4e-5	6.9e-3	1.4e-3
3	310	–2.9e-4	1.6e-4	1.0e-2	1.6e-5	8.0e-3	1.1e-3

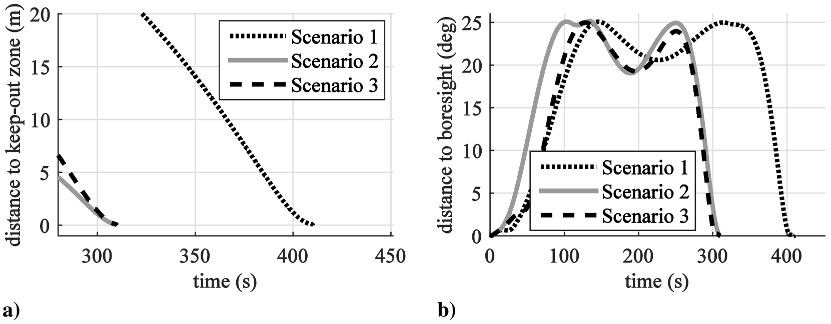

Fig. 5 Path constraints during the maneuvers: a) distance from the keep-out safety zone, and b) angular distance of the target spacecraft center of mass from the chaser sensor boresight.

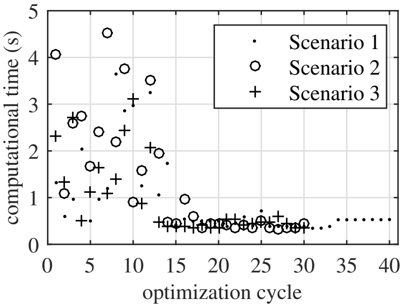

Fig. 6 Computational time required by SNOPT to converge to a solution at each cycle.

$$b_{1,2}=\frac{\ddot{x}_0}{2},\quad b_{2,2}=\frac{\ddot{y}_0}{2},\quad b_{3,2}=\frac{\ddot{z}_0}{2},\quad a_{j,2}=\frac{\ddot{\sigma}^{C}_{j0}}{2},\quad j=1,2,3 \tag{44}$$

The performance index J related to the three test maneuvers is summarized in Table 5. The index J_{GNC} for the controlled trajectory is calculated with Eq. (18) using the controls generated by the guidance system. Similarly, J_{GPOPS} is calculated with Eq. (18) using the optimal controls. Comparison among optimal indexes shows that the trajectories generated by the guidance are near-optimal, with a maximum difference in percentage of 1.1% in terms of optimal performance index occurring in scenario 1.

The reason for these discrepancies in optimality can be understood by comparing the trajectories and controls generated by the guidance system with the solutions of the correspondent optimal control problems. Let us now consider scenario 1, which is subjected to the major difference in optimality. Figure 8 shows the translational and rotational trajectories performed by the chaser spacecraft. At any instant of time, the components of the translational trajectory generated by the guidance closely match the optimal ones (Fig. 8a). In fact, the time histories of the optimal trajectory components present smooth shapes and can be represented precisely by high-order polynomials. On the contrary, as can be observed in Fig. 8b, the rotational trajectories differ remarkably from the optimal ones. In this case, the time histories of the optimal MRP feature several inflection points, which are harder to track with the chosen polynomials. Figure 9 graphically compares the controls generated by the guidance and the optimal controls obtained with GPOPS. The thrust components closely match the optimal ones (Fig. 9a). Owing to the nature of the inverse dynamics, this is the consequence of the precise representation of the translational trajectory with the chosen function. However, significant differences are observed between the control torque curves due to the presence of first-order discontinuities in the time histories of the torques generated by the inverse dynamics (Fig. 9b). As previously discussed, fifth-order polynomials are unable to represent the rotational trajectory of the chaser spacecraft with high precision, and consequently, the controls generated by the inverse dynamics method differ from the optimal controls. At each guidance cycle, the polynomial coefficients are recomputed to minimize the difference between the controls generated by the guidance and the optimal ones (i.e., the performance index of the maneuver is minimum). As a result, first-order discontinuities arise as the controls are updated. Analogous observations for scenarios 2 and 3 hold.

Figure 9b also provides interesting information about the motion of the chaser spacecraft. In the first part of the maneuver, the torque action is moderate, meaning that the chaser approaches the target without large changes in attitude and angular velocity. Only in the last part of the maneuver (about 60 s before the docking), the chaser performs intense angular accelerations to synchronize with the rotational motion of the target.

B. Simulations with Random Initial Conditions

With the goal to investigate the performance of the guidance system under more realistic control application, the SDM-PWM technique described in Sec. IV.B is used to convert the continuous force components into an equivalent sequence of maximum-thrust pulses.

The guidance system has been tested on 500 docking scenarios obtained by varying randomly both the initial relative distance between the spacecraft and the initial attitude and rotation rates of the

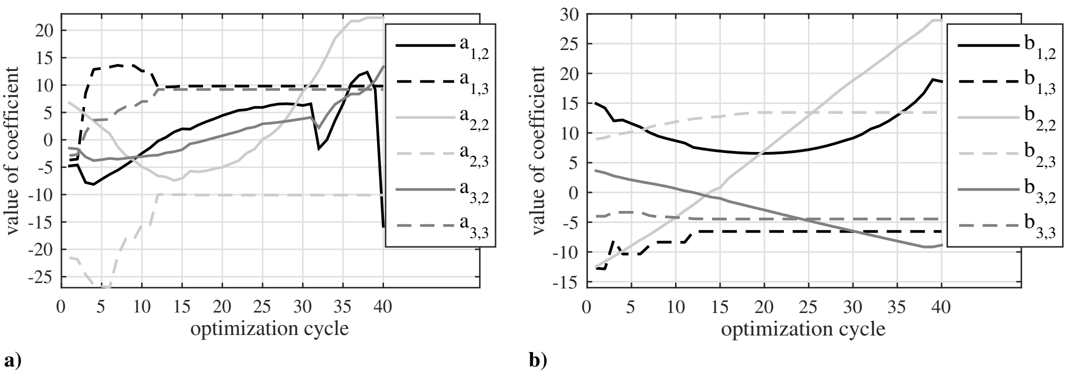

Fig. 7 Evolution of the variable polynomial coefficients optimized by SNOPT during scenario 1: a) attitude, and b) relative distance.

Table 5 Optimal performance index J achieved with GPOPS and with the guidance system

Scenario	J_{GPOPS}, $\mathrm{N}^2 \cdot \mathrm{s}$	J_{GNC}, $\mathrm{N}^2 \cdot \mathrm{s}$	ΔJ, %
1	617.1	624.0	1.1
2	2490.6	2508.6	0.7
3	1331.5	1337.5	0.4

target spacecraft. The orbit of the target spacecraft is circular, with an altitude of 773 km as in Sec. V.A. All the maneuvers start with zero relative translational speed with the chaser at rest (station-keeping configuration) and its sensor boresight pointing the target spacecraft center of mass. The initial conditions are randomly generated within the intervals defined in Table 6 (the initial attitude of the target principal system T is given in terms of Euler angles $[\theta^{\mathrm{T}}_{1_0} \quad \theta^{\mathrm{T}}_{2_0} \quad \theta^{\mathrm{T}}_{3_0}]$), whereas the current state vector $\boldsymbol{x}_t$ and target inertia are the same as in the previous analysis.

Table 7 summarizes the final docking conditions and the performance of the control system after numerical tests on the 500 random scenarios. The final conditions are calculated using Eqs. (11–14) and expressed in the CD coordinate system. Furthermore, axial and radial directions are intended with respect to the target spacecraft docking axis. Because the target center of mass may not always reach the boundary of the chaser sensor FOV, the associated path constraint is considered active when $\alpha_T(\text{peak}) \geq 24.5$ deg. The parameter α_T is calculated using Eq. (15). Remarkably, all the final docking conditions requirements are achieved with high precision, even using the DSM-PWM conversion for the control force. Furthermore, the guidance algorithm enforces the path constraints accurately. In all cases, the peaks of computational time required by SNOPT to converge are lower than 10 s. This result confirms the appropriateness of the choice to update the trajectory at a rate of 0.1 Hz.

C. Sensitivity Analysis to Orbital Perturbations

The most significant orbital disturbances in LEO have been introduced into the Simulink dynamics models [Eqs. (42) and (43)] for both target and chaser spacecraft. In particular, disturbances due to geopotential anomaly, atmospheric drag, and gravitational gradient are considered.

Table 6 Ranges of value for the random initial conditions

Parameter	Range of values
x_0, m	$[-100; -20]$
y_0, m	$[-100; 100]$
z_0, m	$[-20; 20]$
$\omega^{\mathrm{T}}_{x_0}$, $\omega^{\mathrm{T}}_{y_0}$, $\omega^{\mathrm{T}}_{z_0}$, deg/s	$[-4; 4]$
$\theta^{\mathrm{T}}_{1_0}$, $\theta^{\mathrm{T}}_{2_0}$, $\theta^{\mathrm{T}}_{3_0}$, deg	$[-180; 180]$

Table 7 Docking conditions and performance of the guidance obtained with the random scenarios

Parameter	Mean value (3σ)
$\Delta r_{\mathrm{axial}}$, m	2.4e-3 ± 7.0e-3
$\Delta r_{\mathrm{radial}}$, m	3.7e-3 ± 10.1e-3
$\Delta v_{\mathrm{axial}}$, m/s	1.0e-2 ± 0.1e-2
$\Delta v_{\mathrm{radial}}$, m/s	6.7e-4 ± 9.0e-4
$\Delta \theta_{\max}$, deg	2.6e-2 ± 0.51
$\Delta \omega_{\max}$, deg/s	3.4e-2 ± 9.3e-2
$\alpha_{T\,\max}$, deg	25.0 ± 0.2
Minimum distance from keep-out zone, m	1.3e-3 ± 2.2e-3
CPU time (average), s	0.99 ± 1.73
CPU time (peak), s	±3.76

The nonhomogeneous gravitational potential of the Earth is considered up to the harmonic coefficient J_6. In particular, the translational acceleration due to the term J_2 is calculated with the following [39]:

$$\boldsymbol{a}_{J2} = \frac{3J_2\mu r_{\oplus}^2}{2\|\boldsymbol{r}\|^5}\begin{bmatrix} \left(1 - \frac{5r_z^2}{\|\boldsymbol{r}\|^5}\right)r_x \\ \left(1 - \frac{5r_z^2}{\|\boldsymbol{r}\|^5}\right)r_y \\ \left(3 - \frac{5r_z^2}{\|\boldsymbol{r}\|^5}\right)r_z \end{bmatrix} \tag{45}$$

where $r_{\oplus}$ is the average Earth equatorial radius. The expressions for the other acceleration terms until J_6 are analogous to Eq. (45) and can be found in [39].

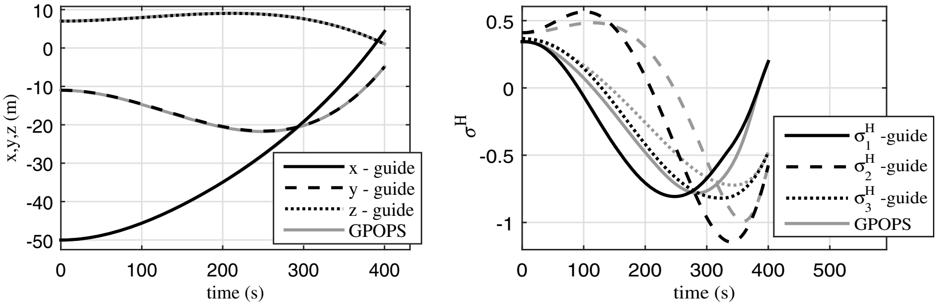

a) b)

Fig. 8 Scenario 1: time history of the translational and rotational components of the chaser trajectory obtained with the guidance system and with GPOPS.

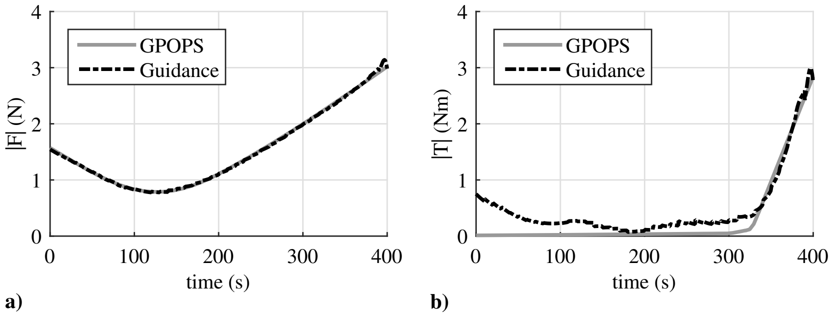

a) b)

Fig. 9 Scenario 1: time histories of the thrust and torque norms generated with the guidance algorithm and GPOPS.

The translational acceleration due to the atmospheric drag is described as [39]

$$\boldsymbol{a}_{\mathrm{drag}} = -\sum_i \frac{1}{2}\rho \frac{\mathrm{C_D} A_i}{m_\mathrm{C}} \|\boldsymbol{v}_{\mathrm{rel}}\| \boldsymbol{v}_{\mathrm{rel}} \tag{46}$$

where the density ρ of the atmosphere is estimated with the exponential model described in [39]. The drag coefficient is $\mathrm{C_D} = 2.2$. The term A_i is the exposed cross-sectional area of the ith surface of the spacecraft defined as the area that is normal to the vehicle velocity vector. The shape of each spacecraft is assumed rectangular parallelepiped. The velocity $\boldsymbol{v}_{\mathrm{rel}}$ denotes the velocity of spacecraft center of mass relative to the rotating atmosphere, and it is defined as

$$\boldsymbol{v}_{\mathrm{rel}} = \dot{\boldsymbol{r}} - \begin{bmatrix} 0 \\ 0 \\ \omega_\oplus \end{bmatrix} \times \boldsymbol{r} \tag{47}$$

where $\omega_\oplus$ is the rotation velocity of the Earth.

The external torque acting on each spacecraft due to the atmospheric drag is given by

$$\boldsymbol{T}_{\mathrm{drag}} = -\sum_i \boldsymbol{L}_i \times \left(\frac{1}{2}\rho C_\mathrm{D} A_i \|\boldsymbol{v}_{\mathrm{rel}}\| \boldsymbol{v}_{\mathrm{rel}}\right) \tag{48}$$

where the displacement vector $\boldsymbol{L}_i$ relative to the surface A_i corresponds to the distance between the spacecraft center of mass and the surface geometric center.

The external torque due to the gravitational gradient is [42]

$$\boldsymbol{T}_{GG} = \frac{3\mu}{\|\boldsymbol{r}\|^5} \begin{bmatrix} (I_{yy}^\mathrm{C} - I_{zz}^\mathrm{C}) r_z r_y \\ (I_{zz}^\mathrm{C} - I_{xx}^\mathrm{C}) r_x r_z \\ (I_{xx}^\mathrm{C} - I_{yy}^\mathrm{C}) r_z r_y \end{bmatrix} \tag{49}$$

Analogous expressions are applied for the target spacecraft.

Under these conditions, the guidance system has been tested on the same random scenarios of Sec. V.B. As can be observed in Table 8, the required final docking conditions are achieved with high precision also in the presence of the orbital perturbations. In fact, by updating the trajectory every 10 s, the effects of the orbital perturbations within this time range are mitigated. However, the orbital perturbations cause an increment of the energy expenditure with respect to the ideal case.

D. Sensitivity Analysis to System Disturbances and Applicability to Noncooperative Maneuvers

The proposed guidance system has been subjected to a sensitivity analysis to study its behavior in presence of model errors and noise in the chaser-target system state vector $\boldsymbol{x}_t$ (see Fig. 3) and therefore its applicability to noncooperative scenarios. Errors in relative distance and translational velocity between spacecraft centers of mass along with errors in target spacecraft principal inertia, angular velocities, and attitude are considered in our analysis. This choice is driven by the fact that these parameters are subjected to major uncertainties during the docking maneuver to a noncooperative target [27,43]. Conversely, angular velocities and attitude of the chaser spacecraft with respect to the ECI coordinate system are usually provided by the inertial measurement unit with higher accuracy [44].

Table 8 Docking conditions and performance of the guidance with the perturbed random scenarios

Parameter	Mean value (3σ)
$\Delta r_{\mathrm{axial}}$, m	3.0e-3 ± 17.0e-3
$\Delta r_{\mathrm{radial}}$, m	4.2e-3 ± 15.0e-3
$\Delta v_{\mathrm{axial}}$, m/s	1.0e-2 ± 0.2e-2
$\Delta v_{\mathrm{radial}}$, m/s	8.0e-4 ± 38.0e-4
$\Delta\theta_{\mathrm{max}}$, deg	3.4e-2 ± 0.79
$\Delta\omega_{\mathrm{max}}$, deg /s	3.9e-2 ± 12.2e-2
$\alpha_{T\,\mathrm{max}}$, deg	25.1 ± 0.3
CPU time (average), s	1.04 ± 1.99
CPU time (peak), s	5.33 ± 4.21
$J_{\mathrm{disturbances}}/J_{\mathrm{ideal}}$, %	1.1 ± 0.5

At this point, it is important to note that the proposed guidance system is a model-based algorithm and requires the knowledge of the target inertia. In the case of noncooperative maneuvers, this parameter can be retrieved from the target spacecraft constructor, as the case of Envisat. When this solution is not available, the target inertia can be estimated onboard the chaser during closed-range observation maneuvers before the docking procedure [45,46]. In both cases, however, the target inertia might be subjected to significant uncertainties.

The sensitivity analysis is performed on reference scenario 1 (data in Table 3) with the following combinations of parameter variation and/or noises: 1) noise on relative distance and relative translational velocity; 2) errors in target spacecraft principal inertia and noise in target spacecraft angular velocity; 3) errors in target spacecraft principal inertia and noise in target spacecraft attitude; and 4) noise on target spacecraft angular velocity and attitude. The choice of these particular combinations is motivated by the synergic correlation between these factors in the rendezvous dynamics model described in Sec. II. In particular, the components x, y, and z of the relative distance and the components $\dot{x}$, $\dot{y}$, and $\dot{z}$ of the relative velocity are coupled in the Clohessy–Wiltshire dynamics [Eq. (1)]. Moreover, the target spacecraft inertia, angular velocity, and attitude are coupled in the attitude dynamics Eqs. (3) and (8). For each category of system disturbances (relative distance, relative velocity, target inertia, target attitude, and target angular velocity), we consider five levels of noise applied to every component of the vector (see Table 9). In this way, $5 \times 5 = 25$ different combinations of noise level for each of the four combinations of disturbances are obtained. For each particular noise combination, scenario 1 is simulated 50 times. Errors in the inertia of the target spacecraft are applied with random signs to I_{xx}^T, I_{yy}^T, and I_{zz}^T at the beginning of each simulation. The noise on the selected components of the state vector is modeled as a white-noise signal. The performance of the guidance system is evaluated in terms of final docking conditions achievement and energy expenditure as in Sec. V.B. Furthermore, to better evaluate the impact of the disturbances, we acknowledge a successful docking when $\|\Delta r_{\mathrm{radial}}\| \leq 0.05$ m, $\Delta v_{\mathrm{radial}}\| \leq 0.01$ m/s, $\|\Delta\theta_{\mathrm{max}}\| \leq 5$ deg, and $\|\Delta\omega_{\mathrm{max}}\| \leq 0.5$ deg /s as in the Orbital Express mission [47].

The guidance loop is again executed at a rate of 0.1 Hz. Moreover, after the last optimization of the trajectory (i.e., 10 s before the docking), the guidance system in Fig. 3 is executed at a rate of 2 Hz, bypassing the call of SNOPT. Notably, this rate still ensures enough time for noncooperative pose estimation [48]. The control time histories are consequently computed using the last optimal varied parameters and the current end-point conditions [Eqs. (23), (24), (31), and (32)]. This procedure can be implemented only after the last optimization of the trajectory because the computation time is mostly used by SNOPT during the nominal execution of the control loop. In this way, we increase the robustness to disturbances because the docking conditions depend on the predicted final state of the target, which is influenced by the propagation of the noise.

Figures 10 and 11 show the effects of the disturbances on final relative attitude and angular velocity between docking points. The

Table 9 Noise levels ($3\boldsymbol{\sigma}$, except for the inertia) of the system disturbances

System disturbance	Noise level
δx, δy, δz, cm	0, 0.5, 1, 2, 4
$\delta\dot{x}$, $\delta\dot{y}$, $\delta\dot{z}$, cm/s	0, 0.1, 0.25, 0.5, 1
δI_{xx}^T, δI_{yy}^T, δI_{zz}^T, %	0, 1, 2, 3, 4
$\delta\boldsymbol{q}^\mathrm{T}(\theta_{123})$, deg	0, 0.25, 0.5, 1, 2
$\delta\boldsymbol{\omega}^\mathrm{T}$, deg /s	0, 0.1, 0.15, 0.2, 0.25

bounded zones in the graphs depict where the docking precision requirements are met. As can be observed in the figures, the precision requirements are respected for every combination of disturbance levels. Moreover, relative attitude and angular velocity are not sensitive to errors in relative distance and velocity between spacecraft centers of mass (Figs. 10a and 11a). In fact, the guidance system imposes the synchronization of the rotational motion between docking points through the conditions in Eqs. (13) and (14), which are independent from distance and velocity between spacecraft.

Figures 12 and 13 illustrate the influence of the disturbances on the final radial distance and velocity between docking points. Once again, the bounded zones in the graphs depict where the docking

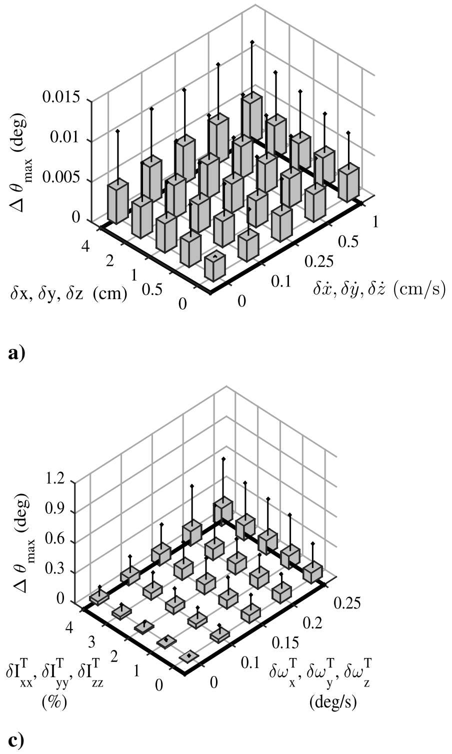

Fig. 10 Final misalignment between docking points for different combinations of system disturbances. The vertical bars denote the mean value, whereas the vertical lines denote the 3σ value.

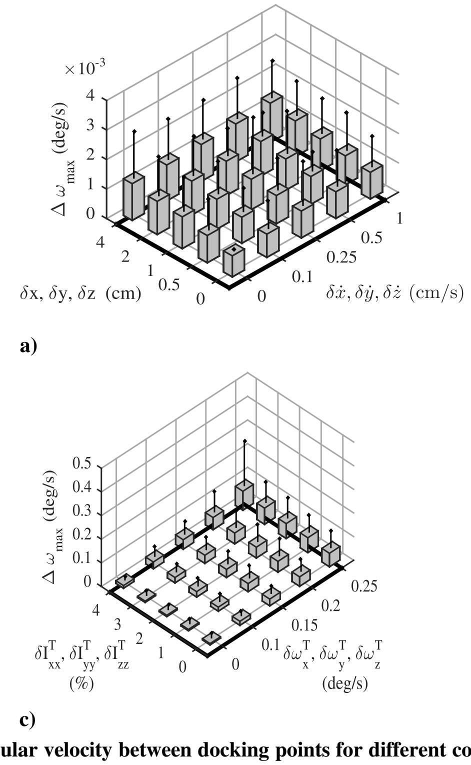

Fig. 11 Final relative angular velocity between docking points for different combinations of system disturbances. The vertical bars denote the mean value, whereas the vertical lines denote the 3σ value.

precision requirements are met. In this case, the final relative velocity results sensitive to the noise in target angular velocity (Figs. 13c and 13d). In fact, as it can be observed in Eq. (12), an error $\delta\boldsymbol{\omega}^{\mathrm{T}}$ in the target angular velocity causes an error in translational velocity proportional to $\delta\boldsymbol{\omega}^{\mathrm{T}} \times \boldsymbol{l}^{\mathrm{T}}$. Clearly, large target spacecraft dimensions amplify the errors in the predicted translational velocity of the target docking port due to the noise on $\boldsymbol{\omega}^{\mathrm{T}}$. Furthermore, disturbances in target angular velocity generate errors in the target final attitude $\boldsymbol{R}_{\mathrm{T}}^{\mathrm{H}}$,

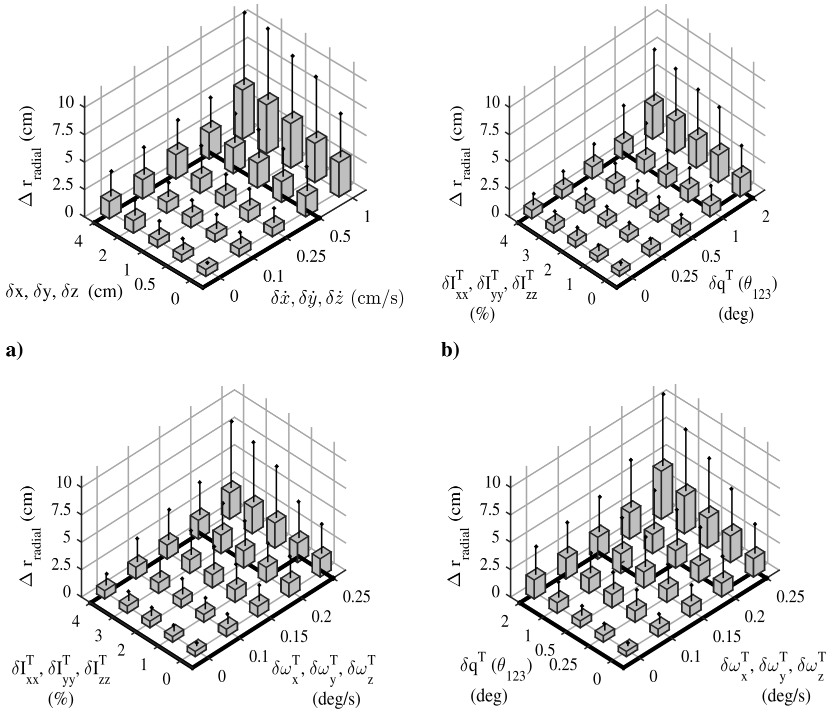

a)

b)

c)

d)

Fig. 12 Final offset (radial direction from the target docking axis) between docking points for different system disturbances. Vertical bars represent the mean value, whereas vertical lines denote the 3σ value.

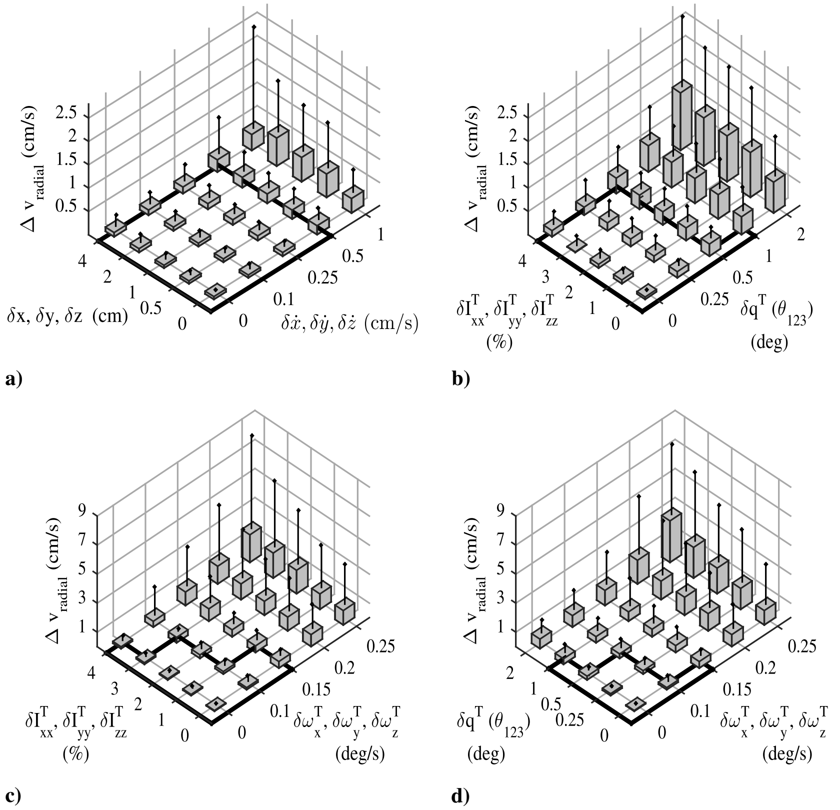

a)

b)

c)

d)

Fig. 13 Final velocity (radial direction from the target docking axis) between docking points for different system disturbances. Vertical bars represent the mean value, whereas vertical lines denote the 3σ value.

which causes a further error in the final translational velocity related to the term $\boldsymbol{\omega}_F^{\mathrm{T}} \times \boldsymbol{R}_{\mathrm{T}}^{\mathrm{H}} \boldsymbol{l}^{\mathrm{T}}$. Also, in this case, large dimension and high rotation rates of the target spacecraft enhance the effect of $\delta\boldsymbol{\omega}^{\mathrm{T}}$. As can be observed from Fig. 13, the precision requirement on radial translational velocity are respected when errors in target angular velocity are limited to $0.1\ \deg/\mathrm{s}\ 3\sigma$ and, at the same time, errors in target inertia and attitude are limited to 2% and 0.5 deg 3σ, respectively. Regarding the final relative distance between docking points, the major offsets are caused by disturbances in relative translational velocity and target angular velocity. In fact, the large errors in radial velocity caused by these disturbances also generate large offsets in the radial direction.

Concerning the optimality of the maneuvers, the presence of system disturbances in the current state vector increases the energy expenditure. In fact, disturbances cause errors in the current estimated state and in the expected final state (obtained by propagation from the current state), and consequently, the resulting trajectories diverge significantly from the optimal one. Noise in the target angular velocity increases the performance index J between 19% 3σ (lowest noise level) and 64% 3σ (highest noise level) with respect to the ideal case without noise, whereas the rest of disturbances case an increment between 5% 3σ and 20% 3σ.

VI. Conclusions

This paper proposes a guidance system for minimum-energy six-degree-of-freedom docking maneuvers between a controlled chaser spacecraft and an uncontrolled target that is in a circular orbit. A direct optimization method is formulated for rapid trajectory generation: polynomials are employed for trajectory representation, the inversion of the system dynamics allows to convert the optimal control problem into an equivalent nonlinear programming problem, and a sequential quadratic programming solver optimizes the unconstrained polynomial coefficients. Such an approach has three main advantages. First, the reduced number of variables to be optimized leads to fast computational speed for trajectory optimization. Second, the reference trajectory and controls are determined by the polynomial coefficients only, enabling easy onboard storage of the solution and rapid control update during the maneuver. Third, the docking-enabling conditions are automatically imposed by simple reconstruction of the polynomials. The closed-loop implementation of such technique includes a combined sigma-delta/pulse-width modulator to convert the continuous control forces generated by the inverse dynamics into sequences of maximum-thrust pulses as well as a low-level attitude and position controllers to sample and actuate the generated control time histories.

In the ideal case of perfect knowledge of the current state vector and target inertia, the proposed guidance system is able to perform near-optimal maneuvers while enforcing all the path constraints and achieving accurate docking conditions. The small difference in optimality is due to slight discrepancies in the chaser attitude trajectory because piecewise polynomials can match the optimal trajectory up to a certain level. The Monte Carlo simulation demonstrates that the guidance scheme, in the same ideal case of perfect knowledge of the target conditions, performs accurate maneuvers in most maneuvering scenarios, also in the presence of orbital perturbations in low Earth orbit.

The applicability of the guidance system to more realistic noncooperative scenarios is tested with a sensitivity analysis via Monte Carlo simulation. We have considered uncertainties on both target inertia and relative state, driven by the fact that these two parameters are the most critical in noncooperative maneuvers. The sensitivity study shows that the proposed guidance system is particularly sensitive to noise in target angular velocity. In fact, this type of disturbance causes significant errors in the final translational velocity between spacecraft docking points. With regard to errors in the target inertia, which might be estimated during the observation phase and therefore subjected to significant uncertainties, the guidance is capable to successfully dock to the target whenever the error is less than 4% of the nominal value.

Even though the proposed trajectory optimization algorithm is a model-based method that requires the knowledge of the target inertia and the current relative state, the proposed closed-loop implementation is able to perform noncooperative maneuvers to uncontrolled tumbling targets under limited errors on target angular velocity and inertia. In fact, the key features that ensure noncooperative applications are 1) onboard/online generation of the docking trajectory using the current state vector and maneuver duration only, 2) prediction of the docking conditions by onboard numerical propagation of the system state, and 3) rapid trajectory and control reshaping based on the latest state estimation.

Appendix: Estimation of the Maneuver Duration

In this Appendix, the pseudocode for the estimation of a feasible maneuver duration is provided. The maneuver duration is calculated in the guidance block during the first execution of the control loop (see Fig. 3).

In the proposed iterative method, a linear acceleration profile is imposed along each axis of the Hill coordinate system. Initially, the acceleration profile is defined on the axis corresponding to the maximum chaser–target distance assuming the action of the maximum available thrust at the beginning and at the end of the maneuver. Subsequently, by propagating the translation dynamics, we verify that the maximum thrust engaged in all components is lower than the maximum thrust available. If this condition is unverified, an acceleration profile with lower magnitude is considered, and the process is repeated. Once the constraint on the maximum thrust level is verified in all three axes, we compute the first estimate of the maneuver duration using the obtained linear thrust profiles. However, we must ensure that the chaser docking point grapples the target docking point at the end of the maneuver. Subsequently, we propagate the rotation dynamics of the target spacecraft for a time larger than the first estimation of the maneuver duration until the target docking point points the chaser at the end of the maneuver. The constraint on the maximum torque level is verified in the same way as for the control thrust.

The case of a rest to rest R-bar approach is presented here, but the proposed procedure can be applied to other maneuvers by changing the end-point conditions and the reference acceleration profile defined in step 1.

Step 1: Impose the following reference linear acceleration profile along the x axis of the Hill coordinate system:

$$\ddot{x}(t) = a_x\left(1 - 2\frac{t}{t_{\mathrm{f}}}\right) \tag{A1}$$

where

$$a_x = -\mathrm{sign}(x_0)K\frac{F_{x,\max}}{m_{\mathrm{C}}} \tag{A2}$$

is the maximum acceleration amplitude, and $K \in [0;1]$ a weighting coefficient. Set a value for K.

Step 2: Impose the end-point condition $x(t_{\mathrm{f}}) = 0$ m to the motion law $x(t)$ obtained from Eq. (A1). Then, compute the first estimate of the maneuver duration with

$$t_{\mathrm{f}}^* = \sqrt{-6\frac{x_0}{a_x}} \tag{A3}$$

Step 3: Impose a linear acceleration profile along the y and z axes of the Hill coordinate system as in Eq. (A1). The required initial accelerations to achieve $y(t_{\mathrm{f}}^*) = 0$ m and $z(t_{\mathrm{f}}^*) = 0$ m are

$$a_y = -6\frac{y_0}{t_{\mathrm{f}}^* 2}, \qquad a_z = -6\frac{z_0}{t_{\mathrm{f}}^{*2}} \tag{A4}$$

Step 4: Evaluate the force components F_x^{H}, F_y^{H}, and F_z^{H} at a given set of instants of time $t_i \in [0, t_{\mathrm{f}}^*]$ using Eq. (26) and the trajectory generated by the linear acceleration profiles. Verify the following conditions:

$$\|F_x^{\mathrm{H}}\| \le F_{x,\max}, \qquad \|F_y^{\mathrm{H}}\| \le F_{y,\max}, \qquad \|F_z^{\mathrm{H}}\| \le F_{z,\max} \tag{A5}$$

If the conditions are verified for each considered instant of time, then go to step 5; otherwise, go back to step 1 and decrease the weighting coefficient K.

Step 5: Set a value for the parameter $\Delta t_{\mathrm{f}} \ge 0$ and estimate the state of the target spacecraft at $t^* = t_{\mathrm{f}}^* + \Delta t_{\mathrm{f}}$ by propagating Eqs. (3) and (8).

Step 6: Compare the final orientation of the coordinate system TD with the initial orientation of the system CD:

$$\boldsymbol{R}_{\mathrm{CD}}^{\mathrm{TD}} = \boldsymbol{R}_{\mathrm{CD}}^{\mathrm{C}} \boldsymbol{R}_{\mathrm{C}}^{\mathrm{H}}(0) \boldsymbol{R}_{\mathrm{H}}^{\mathrm{T}}(t^*) \boldsymbol{R}_{\mathrm{T}}^{\mathrm{TD}} \tag{A6}$$

If the relative orientation in Eq. (A6) is lower than a maximum relative orientation defined by $\boldsymbol{R}_{\mathrm{CD\ max}}^{\mathrm{TD}}$, then go to step 7. Otherwise, go to step 5 and increase Δt_{f}. The matrix $\boldsymbol{R}_{\mathrm{CD\ max}}^{\mathrm{TD}}$ was set using the Euler angles 1-2-3. In our experimental campaign, we limited the maximum relative orientation to ±30 deg for each angle. With this procedure, we ensure that 1) the target is in a favorable configuration for the docking at the end of the maneuver (i.e., the target's auxiliary coordinate system TD points the chaser), and 2) the final orientation of the system TD is similar to the initial orientation of the chaser, resulting in lower control expenditure.

Step 7: Impose the docking-enabling conditions [Eqs. (11–14)] at $t = t^*$. Calculate the expected chaser angular velocity as

$$\begin{bmatrix} \omega_{x_{\mathrm{f}}}^{\mathrm{C}} \\ \omega_{y_{\mathrm{f}}}^{\mathrm{C}} \\ \omega_{z_{\mathrm{f}}}^{\mathrm{C}} \end{bmatrix} = \begin{bmatrix} {}^{\mathrm{H}}\omega_{x_{\mathrm{f}}}^{\mathrm{C}} \\ {}^{\mathrm{H}}\omega_{y_{\mathrm{f}}}^{\mathrm{C}} \\ {}^{\mathrm{H}}\omega_{z_{\mathrm{f}}}^{\mathrm{C}} \end{bmatrix} + \boldsymbol{R}_{\mathrm{H}}^{\mathrm{CD}} \boldsymbol{R}_{\mathrm{CD}}^{\mathrm{C}} \begin{bmatrix} 0 \\ 0 \\ \Omega \end{bmatrix} \tag{A7}$$

where $\boldsymbol{R}_{\mathrm{H}}^{\mathrm{CD}} \boldsymbol{R}_{\mathrm{CD}}^{\mathrm{C}}(t^*)$ due to Eq. (13), and ${}^{\mathrm{H}}\boldsymbol{\omega}_{\mathrm{f}}^{\mathrm{C}}$ is computed from ${}^{\mathrm{H}}\boldsymbol{\omega}_{\mathrm{f}}^{\mathrm{TD}}(t^*)$ via Eq. (14). Compute the expected chaser angular acceleration as

$$\begin{bmatrix} \dot{\omega}_{x_{\mathrm{f}}}^{\mathrm{C}} \\ \dot{\omega}_{y_{\mathrm{f}}}^{\mathrm{C}} \\ \dot{\omega}_{z_{\mathrm{f}}}^{\mathrm{C}} \end{bmatrix} = \boldsymbol{R}_{\mathrm{T}}^{\mathrm{H}}(t^*) \boldsymbol{R}_{\mathrm{H}}^{\mathrm{CD}} \boldsymbol{R}_{\mathrm{CD}}^{\mathrm{C}} \begin{bmatrix} \dot{\omega}_{x_{\mathrm{f}}}^{\mathrm{T}} \\ \dot{\omega}_{y_{\mathrm{f}}}^{\mathrm{T}} \\ \dot{\omega}_{z_{\mathrm{f}}}^{\mathrm{T}} \end{bmatrix} \tag{A8}$$

Step 8: Assuming an initial rest configuration, impose the following linear angular acceleration profile along each axis of the chaser principal coordinate system C:

$$\dot{\omega}_j^{\mathrm{C}}(t) = \frac{\dot{\omega}_{j_{\mathrm{f}}}^{\mathrm{C}} - \dot{\omega}_{j_0}^{\mathrm{C}}}{t^*} t + \dot{\omega}_{j_0}^{\mathrm{C}}, \qquad \omega_j^{\mathrm{C}}(t) = \frac{\dot{\omega}_{j_{\mathrm{f}}}^{\mathrm{C}} - \dot{\omega}_{j_0}^{\mathrm{C}}}{2t^*} t^2 + \dot{\omega}_{j_0}^{\mathrm{C}} t \qquad j = x, y, z \tag{A9}$$

The maneuver duration is t^*. Impose $\omega_j^{\mathrm{C}}(t^*) = \omega_{j\mathrm{f}}^{\mathrm{C}}$ in Eq. (A9), and calculate the initial angular acceleration as

$$\dot{\omega}_{j_0}^{\mathrm{C}} = \frac{2\omega_{j_{\mathrm{f}}}^{\mathrm{C}}}{t^*} - \dot{\omega}_{j_{\mathrm{f}}}^{\mathrm{C}} \qquad j = x, y, z \tag{A10}$$

Step 9: Evaluate the torque components $\mathrm{T}_x^{\mathrm{C}}$, $\mathrm{T}_y^{\mathrm{C}}$, and $\mathrm{T}_z^{\mathrm{C}}$ at a given set of instants of time $t_i \in [0, t^*]$ using Eq. (35) and the imposed angular velocity and acceleration profiles [Eq. (A9)]. At each instant of time, verify the conditions

$$\|\mathrm{T}_x^{\mathrm{C}}\| \le \mathrm{T}_{x,\max}^{\mathrm{C}}, \qquad \|\mathrm{T}_y^{\mathrm{C}}\| \le \mathrm{T}_{y,\max}^{\mathrm{C}}, \qquad \|\mathrm{T}_z^{\mathrm{C}}\| \le \mathrm{T}_{z,\max}^{\mathrm{C}} \tag{A11}$$

If the conditions are verified, then set $t_{\mathrm{f}} = t^*$. Otherwise, go back to step 5 and increase Δt_{f}.

References

[1] Zimpfer, D., Kachmar, P., and Tuohy, S., "Autonomous Rendezvous, Capture and In-Space Assembly: Past, Present and Future," *1st Space Exploration Conference: Continuing the Voyage of Discovery*, AIAA Paper 2005-2523, Jan.–Feb. 2005.
doi:10.2514/6.2005-2523

[2] Saleh, J. H., Lamassoure, E., and Hastings, D. E., "Space Systems Flexibility Provided by On-Orbit Servicing: Part 1," *Journal of Spacecraft and Rockets*, Vol. 39, No. 4, 2002, pp. 551–560.
doi:10.2514/2.3844

[3] Hirzinger, G., Landzettel, K., Brunner, B., Fischer, M., Preusche, C., Reintsema, D., Albu-Schäffer, A., Schreiber, G., and Steinmetz, B. M., "DLR's Robotics Technologies for On-Orbit Servicing," *Advanced Robotics*, Vol. 18, No. 2, pp. 139–174, 2004.
doi:10.1163/156855304322758006

[4] Woffinden, D. C., and Geller, D. K., "Navigating the Road to Autonomous Orbital Rendezvous," *Journal of Spacecraft and Rockets*, Vol. 44, No. 4, 2007, pp. 898–909.
doi:10.2514/1.30734

[5] Oda, M., "ETS-VII: Achievements, Troubles and Future," *Proceeding of the 6th International Symposium on Artificial Intelligence and Robotics and Automation in Space*, Quebec, Canada, June 2001.

[6] Davis, T. M., and Melanson, D., "XSS-10 Microsatellite Flight Demonstration Program Results," *Proceedings of SPIE Conference on Spacecraft Platforms and Infrastructures*, Vol. 5419, SPIE-International Soc. for Optical Engineering, Bellingham, WA, 2004, pp. 16–25.
doi:10.1117/12.544316

[7] Rumford, T. E., "Demonstration of Autonomous Rendezvous Technology (DART) Project Summary," *Proceedings of the Society of Photo-Optical Instrumentation Engineers: Space Systems Technology and Operations*, Vol. 5088, Aug. 2003, pp. 10–19.
doi:10.1117/12.498811

[8] Howard, R. T., and Bryan, T. C., "DART AVGS Flight Results," *Proceedings of the Society of Photo-Optical Instrumentation Engineers*, Vol. 6555, Sensors and Systems for Space Applications, Bellingham, WA, May 2007, pp. 1–10.
doi:10.1117/12.720242

[9] Weismuller, T., and Leinz, M., "GN&C Technology Demonstrated by the Orbital Express Autonomous Rendezvous and Capture Sensor System," *Proceedings of the 29th AAS Guidance and Control Conference*, American Astronautical Soc. Paper 06-016, 2006.

[10] D'Amico, S., Ardaens, J.-S., Gaias, G., Benninghoff, H., Schlepp, B., and Jørgensen, J. L., "Noncooperative Rendezvous Using Angles-Only Optical Navigation: System Design and Flight Results," *Journal of Guidance, Control, and Dynamics*, Vol. 36, No. 6, 2013, pp. 1576–1595.
doi:10.2514/1.59236

[11] Hartley, E. N., Trodden, P. A., Richards, A. G., and Maciejowski, J. M., "Model Predictive Control System Design and Implementation for Spacecraft Rendezvous," *Control Engineering Practice*, Vol. 20, No. 7, pp. 695–713, 2012.
doi:10.1016/j.conengprac.2012.03.009

[12] Singh, L., Bortolami, S., and Page, L., "Optimal Guidance and Thruster Control in Orbital Approach and Rendezvous for Docking Using Model Predictive Control," *AIAA Guidance, Navigation, and Control Conference and Exhibit*, AIAA Paper 2010-7754, Aug. 2010.

[13] Di Cairano, S., Park, H., and Kolmanovsky, I., "Model Predictive Control Approach for Guidance of Spacecraft Rendezvous and Proximity Maneuvering," *International Journal of Robust and Nonlinear Control*, Vol. 22, No. 12, 2012, pp. 1398–1427.
doi:10.1002/rnc.2827

[14] Jacobsen, S., Lee, C., Zhu, C., and Dubowsky, S., "Planning of Safe Kinematic Trajectories for Free Flying Robots Approaching an Uncontrolled Spinning Satellite," *Proceedings of the ASME 27th Annual Biennial Mechanisms and Robotics Conference*, American Soc. of Mechanical Engineers, Fairfield, NJ, 2002, pp. 1145–1151.
doi:10.1115/DETC2002/MECH-34336

[15] Breger, L., and How, J. P., "Safe Trajectories for Autonomous Rendezvous of Spacecraft," *Journal of Guidance, Control, and Dynamics*, Vol. 31, No. 5, 2008, pp. 1478–1489.
doi:10.2514/1.29590

[16] Nolet, S., "Development of a Guidance, Navigation and Control Architecture and Validation Process Enabling Autonomous Docking to a Tumbling Satellite," Ph.D. Dissertation, Dept. of Aeronautics and Astronautics, Massachusetts Inst. of Technology, Cambridge, MA, 2007.

[17] Boyarko, G., Yakimenko, O., and Romano, M., "Optimal Rendezvous Trajectories of a Controlled Spacecraft and a Tumbling Object," *Journal of Guidance, Control, and Dynamics*, Vol. 34, No. 4, 2011,

pp. 1239–1252.
doi:10.2514/1.47645

[18] Boyarko, G., "Spacecraft Guidance Strategies for Proximity Maneuvering and Close Approach with a Tumbling Object," Ph.D. Dissertation, Dept. of Mechanical and Aerospace Engineering, Naval Postgraduate School, Monterey, CA, 2010.

[19] Lu, P., and Liu, X., "Autonomous Trajectory Planning for Rendezvous and Proximity Operations by Conic Optimization," *Journal of Guidance, Control, and Dynamics*, Vol. 36, No. 2, 2013, pp. 375–389.
doi:10.2514/1.58436

[20] Liu, X., and Lu, P., "Solving Nonconvex Optimal Control Problems by Convex Optimization," *Journal of Guidance, Control, and Dynamics*, Vol. 37, No. 3, 2014, pp. 750–765.
doi:10.2514/1.62110

[21] Kobilarov, M., and Pellegrino, S., "Trajectory Planning for Cubesat Short-Time-Scale Proximity Operations," *Journal of Guidance, Control, and Dynamics*, Vol. 37, No. 2, 2014, pp. 566–579.
doi:10.2514/1.60289

[22] Starek, J. A., Acikmese, B., Nesnas, I. A. D., and Pavone, M., *Spacecraft Autonomy Challenges for Next Generation Space Missions*, edited by E. Feron, Vol. 460, Lecture Notes in Control and Information Sciences, Springer, Berlin, 2016, pp. 1–48.

[23] Clohessy, W. H., and Wiltshire, R. S., "Terminal Guidance System for Satellite Rendezvous," *Journal of the Aerospace Sciences*, Vol. 27, No. 9, 1960, pp. 653–674.

[24] Wie, B., *Space Vehicle Dynamics and Control*, AIAA Education Series, AIAA, Reston, VA, 1998, pp. 403–407.

[25] Ventura, J., Romano, M., and Walter, U., "Performance Evaluation of the Inverse Dynamics Method for Optimal Spacecraft Reorientation," *Acta Astronautica*, Vol. 110, May–June 2015, pp. 266–278.
doi:10.1016/j.actaastro.2014.11.041

[26] Shuster, M. D., "A Survey of Attitude Representations," *Journal of Astronautical Sciences*, Vol. 41, No. 4, 1993, pp. 439–517.

[27] Fehse, W., *Automated Rendezvous and Docking of Spacecraft*, Cambridge Univ. Press, Cambridge, England, U.K., 2003, pp. 21–282, Chaps. 2–7.

[28] Yakimenko, O., "Direct Method for Rapid Prototyping of Near-Optimal Aircraft Trajectories," *Journal of Guidance, Control, and Dynamics*, Vol. 23, No. 5, 2000, pp. 865–875.
doi:10.2514/2.4616

[29] Liu, H., Lai, X., and Wu, W., "Time-Optimal and Jerk-Continuous Trajectory Planning for Robot Manipulators with Kinematics Constraints," *Robotics and Computer-Integrated Manufacturing*, Vol. 19, No. 2, 2013, pp. 309–317.
doi:10.1016/j.rcim.2012.08.002

[30] Gill, P. E., Murray, W., and Saunders, M. A., "SNOPT: An SQP Algorithm for Large-Scale Constrained Optimization," *SIAM Review*, Vol. 47, No. 1, March 2005, pp. 99–131.
doi:10.1137/S0036144504446096

[31] Betts, J. T., and Gablonsky, J. M., "A Comparison of Interior Point and SQP Methods on Optimal Control Problems," Boeing Phantom Works, Mathematics and Computing Technology, Rept. M&CT-TECH-02-004, Seattle, WA, March 2002.

[32] Colodro, F., Torralba, A., and Laguna, M., "Continuous-Time Sigma-Delta Modulator with an Embedded Pulsewidth Modulation," *IEEE Transaction on Circuits and Systems.* , Vol. 55, No. 3, 2008, pp. 775–785.

[33] Colodro, F., and Torralba, A., "Pulse-Width Modulation in Sigma-Delta Modulators," *Proceedings of 2010 IEEE International Symposium on Circuits and Systems*, IEEE Publ., Piscataway, NJ, 2010, pp. 1081–1084.

[34] Holtz, J., "Pulsewidth Modulation for Electronic Power Conversion," *Proceedings of the IEEE*, Vol. 82, No. 9, 1994, pp. 1194–1214.

[35] Rupp, T., Boge, T., Kiehling, R., and Sellmaier, F., "Flight Dynamics Challenges of the German On-Orbit Servicing Mission DEOS," *21st International Symposium on Space Flight Dynamics (ISSFD)*, French Space Agency, Toulouse, France, 2009.

[36] Virgili, B. B., Lemmens, S., and Krag, H., "Investigation on Envisat Attitude Motion," European Space Agency, Noordwijk, The Netherland, May 2014, https://indico.esa.int/indico/event/46/material/slides/6.pdf [retrieved July 2014].

[37] "Envisat-1: Mission and System Summary," European Space Agency, Noordwijk, The Netherlands, March 1998.

[38] *Matlab Version 2013b User Manual*, Mathworks, Natick, MA, 2013.

[39] Vallado, D. A., *Fundamentals of Astrodynamics and Applications*, Microcosm Press, New York, 2007, Chap. 8.

[40] Kucharski, D., et al., "Attitude and Spin Period of Space Debris Envisat Measured by Satellite Laser Ranging," *IEEE Transactions on Geoscience and Remote Sensing*, Vol. 52, No. 2, Dec. 2014, pp. 7651–7657.
doi:10.1109/TGRS.2014.2316138

[41] Patterson, M. A., and Rao, A. V., "GPOPS II: A MATLAB Software for Solving Multiple-Phase Optimal Control Problems Using hp-Adaptive Gaussian Quadrature Collocation Methods and Sparse Nonlinear Programming," *ACM Transactions on Mathematical Software*, Vol. 39, No. 3, 2013, pp. 1–41.
doi:10.1145/0000000.0000000

[42] Walter, U., *Astronautics: The Physics of Space Flight*, 2nd ed., Wiley, Weinheim, Germany, 2008, pp. 536–538, Chap. 15.

[43] Hillenbrand, U., and Lampariello, R., "Motion and Parameter Estimation of a Free-Floating Space Object from Range Data for Motion Prediction," *8th International Symposium on Artificial Intelligence, Robotics, and Automation in Space (i-SAIRAS 2005)*, Sept. 2005.

[44] Woodman, O. J., "An Introduction to Inertial Navigation," Univ. of Cambridge, TR 696, Computer Lab., Cambridge, England, U.K., 2007.

[45] Tweddle, B. E., "Computer Vision-Based Localization and Mapping of an Unknown, Uncooperative and Spinning Target for Spacecraft Proximity Operations," Ph.D. Dissertation, Dept. of Aeronautics and Astronautics, Massachusetts Inst. of Technology, Cambridge, MA, 2013.

[46] Yu, F., He, Z., Qiao, B., and Yu, X., "Stereo-Vision-Based Relative Pose Estimation for the Rendezvous and Docking on Noncooperative Satellites," *Mathematical Problems in Engineering*, Vol. 2014, Nov. 2014, pp. 1–12.
doi:10.1155/2014/461283

[47] Christiansen, S., and Nilson, T., "Docking System Mechanism Utilized on Orbital Express Program," *Proceedings of the 39th Aerospace Mechanisms Symposium*, Lockheed Martin Space Systems Company, Sunnyvale, CA, May 2008; NASA CP-2008-215252, pp. 207–219.

[48] Ventura, J., Fleischner, A., and Walter, U., "Pose Tracking of a Noncooperative Spacecraft During Docking Maneuvers Using a Time-of-Flight Sensor," *AIAA Guidance, Navigation and Control Conference*, AIAA Paper 2016-0875, Jan. 2016.

This article has been cited by:

1. Bang-Zhao Zhou, Xiao-Feng Liu, Guo-Ping Cai. 2020. Motion-planning and pose-tracking based rendezvous and docking with a tumbling target. *Advances in Space Research* **65**:4, 1139-1157. [Crossref]
2. Abin Alex Pothen, Steve Ulrich. Pose Tracking Control for Spacecraft Proximity Operations Using the Udwadia-Kalaba Framework . [Abstract] [PDF] [PDF Plus]
3. Ying Chen, Zhen He, Shunli Li. 2019. Horizon-based lazy optimal RRT for fast, efficient replanning in dynamic environment. *Autonomous Robots* **43**:8, 2271-2292. [Crossref]
4. Qi Li, Jianping Yuan, Bo Zhang, Huan Wang. 2019. Artificial potential field based robust adaptive control for spacecraft rendezvous and docking under motion constraint. *ISA Transactions* **95**, 173-184. [Crossref]
5. Qi Li, Jianping Yuan, Bo Zhang. 2019. Extended state observer based output control for spacecraft rendezvous and docking with actuator saturation. *ISA Transactions* **88**, 37-49. [Crossref]
6. Renato Volpe, Christian Circi. 2019. Optical-aided, autonomous and optimal space rendezvous with a non-cooperative target. *Acta Astronautica* **157**, 528-540. [Crossref]
7. Xun Wang, Zhaokui Wang, Yulin Zhang. 2019. Automated Orbital Transfer and Hovering Control Using Artificial Potential. *Mathematical Problems in Engineering* **2019**, 1-16. [Crossref]
8. Xun Wang, Zhaokui Wang, Yulin Zhang. 2018. Model Predictive Control to Autonomously Approach a Failed Spacecraft. *International Journal of Aerospace Engineering* **2018**, 1-18. [Crossref]
9. Kai Zhang, Guangren Duan, Mingda Ma. 2018. Adaptive sliding-mode control for spacecraft relative position tracking with maneuvering target. *International Journal of Robust and Nonlinear Control* **28**:18, 5786-5810. [Crossref]
10. Sumant Sharma, Jacopo Ventura, Simone D'Amico. 2018. Robust Model-Based Monocular Pose Initialization for Noncooperative Spacecraft Rendezvous. *Journal of Spacecraft and Rockets* **55**:6, 1414-1429. [Abstract] [Full Text] [PDF] [PDF Plus]
11. Christopher Jewison, David W. Miller. 2018. Probabilistic Trajectory Optimization Under Uncertain Path Constraints for Close Proximity Operations. *Journal of Guidance, Control, and Dynamics* **41**:9, 1843-1858. [Abstract] [Full Text] [PDF] [PDF Plus]
12. Ding Zhou, Zhenhua Yu, Yanquan Zhang, Shunli Li. Rapidly Sampling-Based Trajectory Planning for Spacecraft Proximity 116-120. [Crossref]
13. Costantinos Zagaris, Marcello Romano. 2018. Reachability Analysis of Planar Spacecraft Docking with Rotating Body in Close Proximity. *Journal of Guidance, Control, and Dynamics* **41**:6, 1416-1422. [Citation] [Full Text] [PDF] [PDF Plus]
14. David Charles Sternberg, David Miller. 2018. Parameterization of Fuel-Optimal Synchronous Approach Trajectories to Tumbling Targets. *Frontiers in Robotics and AI* **5**. . [Crossref]
15. Josep Virgili-Llop, Costantinos Zagaris, Hyeongjun Park, Richard Zappulla, Marcello Romano. 2018. Experimental evaluation of model predictive control and inverse dynamics control for spacecraft proximity and docking maneuvers. *CEAS Space Journal* **10**:1, 37-49. [Crossref]
16. Sabrina Corpino, Stefano Mauro, Stefano Pastorelli, Fabrizio Stesina, Gabriele Biondi, Loris Franchi, Tharek Mohtar. 2018. Control of a Noncooperative Approach Maneuver Based on Debris Dynamics Feedback. *Journal of Guidance, Control, and Dynamics* **41**:2, 431-448. [Abstract] [Full Text] [PDF] [PDF Plus]
17. Costantinos Zagaris, Marcello Romano. Applied Reachability Analysis for Spacecraft Rendezvous and Docking with a Tumbling Object . [Citation] [PDF] [PDF Plus]